

<sub>1</sub> Physics-Infused Reduced-Order Modeling for Analysis of  
<sub>2</sub> Ablating Hypersonic Thermal Protection Systems

<sub>3</sub>

<sub>4</sub> November 16, 2025

<sub>5</sub> **Abstract**

<sub>6</sub> This work presents a *physics-infused reduced-order modeling* (PIROM) framework  
<sub>7</sub> towards the design, analysis, and optimization of non-decomposing ablating hyper-  
<sub>8</sub> sonic thermal protection systems (TPS). It is demonstrated via the modeling of tran-  
<sub>9</sub> sient thermo-ablative behavior of non-decomposing multi-layered hypersonic TPS. The  
<sub>10</sub> PIROM architecture integrates a reduced-physics backbone, based on the lumped-  
<sub>11</sub> capacitance model (LCM), with data-driven correction dynamics formulated via a  
<sub>12</sub> coarse-graining approach rooted in the Mori-Zwanzig formalism. The LCM is coupled  
<sub>13</sub> to a surface velocity model (SVM) to capture the recession of the ablating TPS as a  
<sub>14</sub> function of the surface temperature. While the LCM and SVM capture the dominant  
<sub>15</sub> physics of the ablating TPS response, the correction terms compensate for residual  
<sub>16</sub> dynamics arising from higher-order non-linear interactions and heterogeneities across  
<sub>17</sub> material layers. The PIROM consistently achieves errors below 1% for a wide range of  
<sub>18</sub> extrapolative settings of design parameters involving time-and-space varying boundary  
<sub>19</sub> conditions and SVM models, and improves by  $x\%$  over the LCM alone. Moreover, the  
<sub>20</sub> PIROM delivers online evaluations that are two orders of magnitude faster than the  
<sub>21</sub> full-order model (FOM). These results demonstrate that PIRO effectively reconciles  
<sub>22</sub> the trade-offs between accuracy, generalizability, and efficiency, providing a promising

23 framework for optimizing multi-physical dynamical systems, such as TPS under diverse  
24 operating conditions.

## 25 1 Introduction

26 At hypersonic speeds, aerospace vehicles experience extreme aero-thermo-dynamic environ-  
27 ments that require specialized thermal protection systems (TPS) to shield internal sub-  
28 structures, electronics, and possibly crew members from the intense aerodynamic heating.  
29 The TPS is often composed of ablating materials – a high-temperature capable fibrous  
30 material injected with a resin that fills the pore network and strengthens the compos-  
31 ite [Amar2016](#). The TPS design promotes the exchange of mass through thermal and  
32 chemical reactions (i.e., pyrolysis), effectively mitigating heat transfer to the sub-structures.

33 As a result, accurate prediction for the ablating TPS response under extreme hyper-  
34 sonic heating becomes fundamental to ensuring survivability, performance, and safety of  
35 hypersonic vehicles. Not only is it necessary to assess the performance of the thermal man-  
36 agement systems, but also the shape changes of the vehicle’s outer surface induced by the  
37 ablating material, and its impact on the aerodynamics, structural integrity, and controlla-  
38 bility. Nonetheless, high-fidelity simulations of ablating TPS remains a formidable challenge  
39 both theoretically and computationally.

40 Unfortunately, high-fidelity simulations of ablating TPS remains a formidable challenge  
41 both theoretically and computationally.

42 On the theoretical side, the thermo-chemical reactions, coupled with the irregular pore  
43 network structure, translate into simplifying assumptions to reduce non-linearities, and make  
44 the resulting equations more amenable for engineering application and design analysis [x](#).  
45 For instance, one of the most notable codes is the one-dimensional [CMA](#) code that was  
46 developed by Aerotherm Corporation in the 1960s [Howard2015](#). Despite its practical use  
47 in...

48 Another example is the CHarring Ablator Response (CHAR) ablation code, which ignores  
49 elemental decompositions of the pyrolyzing gases, assumes the gases to be a mixture of perfect  
50 gases in thermal equilibrium, and assumes no reaction or condensation with the porous  
51 network [1].

52 In sum, the objectives of this work are as follows:

- 53 1. Extend the previous formulation from Ref. [12] to model the transient thermo-ablative  
54 response of multi-layered hypersonic TPS through a systematic coarse-graining proce-  
55 dure based on the Mori-Zwanzig formalism.
- 56 2. Benchmark the accuracy, generalizability, and computational efficiency of the PIROM  
57 against the RPM and the high-fidelity FEM solutions of ablating TPS, thus demon-  
58 strating the PIROM’s potential to solve the ITM in complex multi-physical non-linear  
59 dynamical systems.

## 60 **2 Modeling of Ablating Thermal Protection Systems**

61 This section presents the problem of modeling a non-decomposing ablating TPS subjected to  
62 extreme hypersonic heating. Two different but mathematically connected solution strategies  
63 are provided: (1) a high-fidelity full-order model (FOM) based on a finite element method  
64 (FEM), and (2) a low-fidelity reduced-physics model (RPM) based on a lumped capacitance  
65 model (LCM) and a one-dimensional surface velocity model (SVM). The FOM is compu-  
66 tationally expensive but provides the highest fidelity, while the RPM is computationally  
67 efficient but has low predictive fidelity; both models are amenable to high-dimensional de-  
68 sign variables. The RPM is used in the subsequent sections for deriving the PIROM.

### 69 **2.1 Governing Equations**

70 The multi-physics for a non-decomposing ablating TPS involves the *energy equation* which  
71 models the transient heat conduction inside the TPS, and the *pseudo-elasticity equation*,

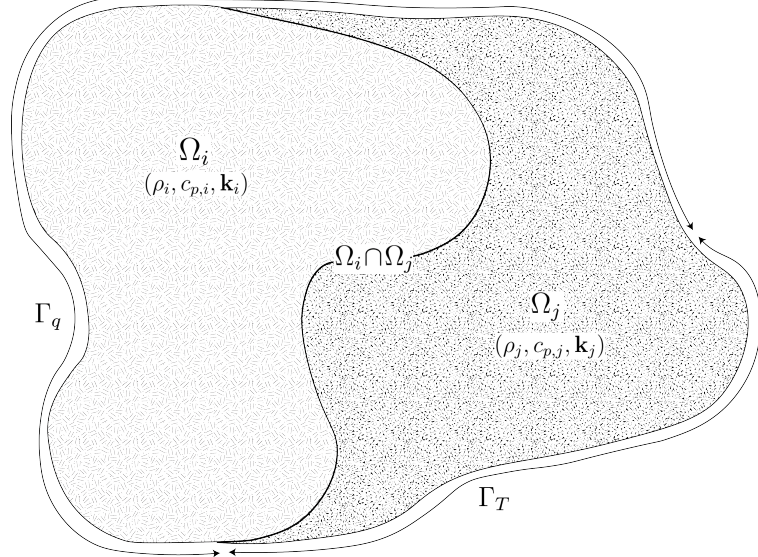


Figure 1: General domain  $\Omega$  with prescribed Neumann and Dirichlet boundary conditions on  $\Gamma_q$  and  $\Gamma_T$ . Mesh displacement  $w(x, t)$  occurs on the  $\Gamma_q$  boundary.

72 which models the mesh motion due to surface recession. The governing PDEs for the ablating  
 73 TPS are summarized in this section.

74 **2.1.1 Energy Equation**

75 Consider a generic domain  $\Omega \subset \mathbb{R}^d$ ,  $d = 2$  or  $3$ , illustrated in Fig. 1. Let  $\partial\Omega = \Gamma_q \cup \Gamma_T$  and  
 76  $\Gamma_q \cap \Gamma_T = \emptyset$ , where a Neumann  $q_b(x, t)$  boundary condition is prescribed on the  $\Gamma_q$  boundary,  
 77 and represents the surface exposed to the hypersonic boundary layer. The Dirichlet  $T_b(x, t)$   
 78 boundary condition is prescribed on the boundary  $\Gamma_T$ . The TPS is divided into  $N$  non-  
 79 overlapping components  $\{\Omega_i\}_{i=1}^N$ , as illustrated in Fig. 1 for  $N = 2$ . The  $i$ -th component  $\Omega_i$   
 80 is associated with material properties  $(\rho_i, c_{p,i}, \mathbf{k}_i)$ , that are assumed to be continuous within  
 81 one component, and can be discontinuous across two neighboring components.

82 The transient heat conduction is described by the energy equation,

$$\rho c_p \left( \frac{\partial T}{\partial t} + \tilde{\mathbf{v}}(x, t) \cdot \nabla T \right) - \nabla \cdot (\mathbf{k} \nabla T) = 0, \quad x \in \Omega \quad (1a)$$

$$-\mathbf{k} \nabla T \cdot \mathbf{n} = q_b(x, t), \quad x \in \Gamma_q \quad (1b)$$

$$T(x, t) = T_b(x, t), \quad x \in \Gamma_T \quad (1c)$$

$$T(x, 0) = T_0(x), \quad x \in \Omega \quad (1d)$$

83 where the density  $\rho$  is constant, while the heat capacity  $c_p$  and thermal conductivity  $\mathbf{k} \in \mathbb{R}^{d \times d}$   
 84 may depend on temperature. In the order they appear, the terms in eq. (1a) include, the  
 85 unsteady energy storage, heat conduction, temperature advection due to mesh motion, and  
 86 source terms due to boundary conditions. The boundary conditions for the energy equation  
 87 includes Neumann eq. (1b) and Dirichlet eq. (1c) on  $\Gamma_T$ .

88 An Abirtrary Lagrangian-Eulerian (ALE) description is used to account for mesh motion  
 89 due to surface recession, where  $\tilde{\mathbf{v}}(x, t)$  is the relative velocity of the material with respect to  
 90 the mesh,

$$\tilde{\mathbf{v}}(x, t) = \mathbf{v}_s(x, t) - \mathbf{v}_m(x, t) \quad (2)$$

91 where  $\mathbf{v}_s(x, t)$  and  $\mathbf{v}_m(x, t)$  are the physical material velocity and mesh velocity, respectively.  
 92 In this work, the physical material velocity is assumed to be zero, i.e.,  $\mathbf{v}_s(x, t) = \mathbf{0}$ , and thus  
 93 the relative velocity is simply the negative of the mesh velocity,  $\tilde{\mathbf{v}}(x, t) = -\mathbf{v}_m(x, t)$ .

<sup>94</sup> **2.1.2 Pseudo-Elasticity Equation**

<sup>95</sup> The mesh motion is described by the steady-state pseudo-elasticity equation without body  
<sup>96</sup> forces,

$$\nabla \cdot \boldsymbol{\sigma}(\mathbf{w}) = \mathbf{0}, \quad \forall t \in \mathcal{T}, \mathbf{x} \in \Omega \quad (3a)$$

$$\mathbf{w}(\mathbf{x}, t) = \mathbf{w}_q(\mathbf{x}, t), \quad \forall t \in \mathcal{T}, \mathbf{x} \in \Gamma_q \quad (3b)$$

$$\mathbf{w}(\mathbf{x}, t) = \mathbf{0}, \quad \forall t \in \mathcal{T}, \mathbf{x} \notin \Gamma_q \quad (3c)$$

$$\mathbf{w}(\mathbf{x}, 0) = \mathbf{0}, \quad \forall \mathbf{x} \in \Omega \quad (3d)$$

<sup>97</sup> where the stress tensor  $\boldsymbol{\sigma}$  is related to the strain tensor  $\boldsymbol{\epsilon}(\mathbf{w})$  through Hooke's law,

$$\boldsymbol{\sigma}(\mathbf{w}) = \mathbb{D} : \boldsymbol{\epsilon}(\mathbf{w})$$

<sup>98</sup> where  $\mathbb{D}$  is the fourth-order positive definite elasticity tensor, and ":" is the double con-  
<sup>99</sup> traction of the full-order tensor  $\mathbb{D}$  with the second-order tensor  $\boldsymbol{\epsilon}$ . The elasticity tensor  
<sup>100</sup> ordinarily possess a number of symmetries, effectively reducing the number of components  
<sup>101</sup> that describe it [2]. The symmetric strain tensor  $\boldsymbol{\epsilon}$  measures the deformation of the mesh  
<sup>102</sup> due to displacements  $\mathbf{w}(x, t)$ , and is defined as,

$$\boldsymbol{\epsilon}(\mathbf{w}) = \frac{1}{2} (\nabla \mathbf{w} + \nabla \mathbf{w}^\top)$$

<sup>103</sup> The "material" properties for the mesh are chosen to tailor the mesh deformation, and need  
<sup>104</sup> not represent the actual material being modeled [1].

<sup>105</sup> For the pseudo-elasticity equations, the boundary conditions include prescribed displace-  
<sup>106</sup> ments  $\mathbf{w}_q(x, t)$  on the heated boundary  $\Gamma_q$  in eq. (3b), and zero displacements on the unheated  
<sup>107</sup> boundaries in eq. (3c). The initial condition for the mesh displacements is zero in eq. (3d).  
<sup>108</sup> Particularly, the surface velocity due to the ablating material is a function of the surface

<sup>109</sup> temperature  $T_q(x, t)$  for  $x \in \Gamma_q$  on the heated boundary. For the  $i$ -th material component,  
<sup>110</sup> the mesh velocity on the heated boundary is imposed based on the following relation,

$$\hat{\mathbf{n}} \cdot \mathbf{v}_m(x, t) = f(T_q(x, t)), \quad x \in \Gamma_q \quad (4)$$

<sup>111</sup> where  $\hat{\mathbf{n}}$  is the unit normal vector on the heated boundary  $\Gamma_q$ , and  $f$  is a function obtained  
<sup>112</sup> from tabulated data for the material, commonly referred to as a B' table [1]. The B' table  
<sup>113</sup> provides a model for the recession velocity as a function of the surface temperature, and is  
<sup>114</sup> pre-computed based on high-fidelity simulations of the ablation process for a one-dimensional  
<sup>115</sup> slab of the material, and is independent of the TPS geometry. Provided the surface velocity,  
<sup>116</sup> the boundary condition in eq. (5) for the mesh displacements are computed by integrating  
<sup>117</sup> the surface velocity over time,

$$\mathbf{w}_q(x, t) = \int_0^t \mathbf{v}_m(x, \tau) d\tau \quad (5)$$

## <sup>118</sup> 2.2 Full-Order Model: Finite-Element Method

<sup>119</sup> To obtain the full-order numerical solution, the *energy equation* is spatially discretized using  
<sup>120</sup> variational principles of the Discontinuous Galerkin (DG) method [5]. Note that the choice  
<sup>121</sup> of DG approach is mainly for theoretical convenience, and is exclusively performed on the  
<sup>122</sup> energy equation, as it is the surface temperature that drives the ablation process. The  
<sup>123</sup> equivalence between DG and FEM is noted upon their convergence. For the *pseudo-elasticity*  
<sup>124</sup> *equation* standard FEM is used to compute the mesh displacements based on the surface  
<sup>125</sup> temperature provided by the DG solution of the energy equation [2].

<sup>126</sup> Consider a conforming mesh partition domain, where each element belongs to one and  
<sup>127</sup> only one component. Denote the collection of all  $M$  elements as  $\{E_i\}_{i=1}^M$ . In an element  $E_i$ ,  
<sup>128</sup> its shared boundaries with another element  $E_j$ , Neumann BC, and Dirichlet BC are denoted  
<sup>129</sup> as  $e_{ij}$ ,  $e_{iq}$ , and  $e_{iT}$ , respectively. Lastly,  $|e|$  denotes the length ( $n_d = 2$ ) or area ( $n_d = 3$ ) of a

<sup>130</sup> component boundary  $e$ .

<sup>131</sup> For the  $i$ -th element, use a set of  $P$  trial functions, such as polynomials, to represent the  
<sup>132</sup> temperature distribution,

$$T_i(x, t) = \sum_{l=1}^P \phi_l^i(x) u_l^i(t) \equiv \boldsymbol{\phi}_i^\top(x) \mathbf{u}_i(t), \quad i = 1, 2, \dots, M \quad (6)$$

<sup>133</sup> Without loss of generality, the trial functions are assumed to be orthogonal, so that,

$$\int_{E_i} \phi_l^i(x) \phi_k^i(x) d\Omega = 0, \quad l \neq k$$

<sup>134</sup> where  $\delta_{lk}$  is the Kronecker delta function. Furthermore, for simplicity, choose  $\phi_1^i = 1$ . Thus,  
<sup>135</sup> by orthogonality,

$$\int_{E_i} \phi_1^i(x) d\Omega = |E_i|, \quad \int_{E_i} \phi_k^i(x) d\Omega = 0, \quad k = 2, 3, \dots, P$$

<sup>136</sup> Under the choice of basis functions,  $u_1^i$  is simply the average temperature of element  $E_i$ ,  
<sup>137</sup> denoted as  $\bar{u}_i$ .

<sup>138</sup> By standard variational processes, e.g., [5], the element-wise governing equation is de-  
<sup>139</sup> noted as,

$$\mathbf{A}_i \dot{\mathbf{u}}_i = (\mathbf{B}_i + \mathbf{C}_i) \mathbf{u}_i + \sum_{j \in \mathcal{N}_i \cup \{T_b\}} (\mathbf{B}_{ij}^i \mathbf{u}_i + \mathbf{B}_{ij}^j \mathbf{u}_j) + \mathbf{f}_i(t), \quad \text{for } i = 1, 2, \dots, M \quad (7)$$

<sup>140</sup> which is collected as the following ODE for all the elements in the mesh,

$$\mathbf{A}(\mathbf{u}) \dot{\mathbf{u}} = [\mathbf{B}(\mathbf{u}) + \mathbf{C}(\mathbf{u})] \mathbf{u} + \mathbf{f}(t) \quad (8)$$

<sup>141</sup> where  $\mathbf{u} = [\mathbf{u}_1, \mathbf{u}_2, \dots, \mathbf{u}_M]^\top \in \mathbb{R}^{MP}$  includes all the DG variables,  $\mathbf{f} \in \mathbb{R}^{MP}$  is the exter-  
<sup>142</sup> nal forcing, and the system matrices  $\mathbf{A}$ ,  $\mathbf{B}$ , and  $\mathbf{C}$  are the matrices due to heat capacity,  
<sup>143</sup> heat conduction, and temperature advection due to mesh motion, respectively. A detailed

<sup>144</sup> derivation of eqs. (7) and (8) and their matrices is provided in Appendix A.

## <sup>145</sup> 2.3 Reduced-Physics Model

<sup>146</sup> The RPM for predicting the response of the ablating TPS consists of two components: (1)  
<sup>147</sup> the *lumped-capacitance model* (LCM), and (2) the *surface velocity model* (SVM). The LCM is  
<sup>148</sup> described as a first-order system of ODEs for predicting the average temperatures inside the  
<sup>149</sup> components of the TPS, and provides a low-fidelity (under estimate) for the component's  
<sup>150</sup> surface temperature. The SVM provides a relation between the surface temperature and  
<sup>151</sup> the surface recession velocity based on pre-computed B' tables for the material, enabling the  
<sup>152</sup> computation of one-dimensional surface displacements. The LCM and SVM are combined to  
<sup>153</sup> define the RPM, providing low-fidelity estimates for the temperatures and surface recession  
<sup>154</sup> of the ablating TPS.

### <sup>155</sup> 2.3.1 Lumped Capacitance Model

<sup>156</sup> A general form of the LCM is provided in this section; details regarding the derivation for  
<sup>157</sup> the four-component TPS in Fig. ?? are provided in Appendix A. The LCM is a classical  
<sup>158</sup> physics-based low-order model for predicting the temporal variation of average temperature  
<sup>159</sup> in multiple interconnected components [7]. The LCM is derived at the component level from  
<sup>160</sup> a point of view of energy conservation, and leads to the following system of ODEs for the  
<sup>161</sup> average temperatures on the components,

$$\bar{\mathbf{A}}\dot{\bar{\mathbf{u}}} = \bar{\mathbf{B}}\bar{\mathbf{u}} + \bar{\mathbf{f}}(t) \quad (9)$$

<sup>162</sup> Where the states and inputs,

$$\bar{\mathbf{u}} = [\bar{u}_1, \bar{u}_2, \dots, \bar{u}_N]^\top \in \mathbb{R}^N, \quad \bar{\mathbf{f}} = [\bar{f}_1, \bar{f}_2, \dots, \bar{f}_N]^\top \in \mathbb{R}^N \quad (10)$$

<sup>163</sup> include the average temperatures  $\bar{\mathbf{u}}$  and spatially-integrated inputs  $\bar{\mathbf{f}}$  for the  $N$  components.  
<sup>164</sup> For  $i, j = 1, 2, \dots, N$  the  $(i, j)$ -th elements of the  $\bar{\mathbf{A}} \in \mathbb{R}^{N \times N}$ ,  $\bar{\mathbf{B}} \in \mathbb{R}^{N \times N}$ , and  $\bar{\mathbf{f}} \in \mathbb{R}^N$   
<sup>165</sup> matrices are given by,

$$\bar{A}_i = \begin{cases} \int_{\Omega_i} \rho c_p d\Omega_i, & i = j \\ 0, & i \neq j \end{cases}, \quad \bar{B}_{ij} = \begin{cases} \sum_{j \in \mathcal{N}_i \cup \{T_b\}} \bar{B}_{ij}^i, & i = j \\ \bar{B}_{ij}^{(j)}, & i \neq j \end{cases}, \quad (11a)$$

$$\mathbf{f}_i = \begin{cases} |e_{iq}| \bar{q}_i + \frac{|e_{iT}|}{R_i} \bar{T}_i, & i = j \\ 0, & i \neq j \end{cases} \quad (11b)$$

<sup>166</sup> where,

$$\bar{q}_i = \frac{1}{|e_{iq}|} \int_{e_{iq}} q_b de_{iq}, \quad \bar{T}_i = \frac{1}{|e_{iT}|} \int_{e_{iT}} T_b de_{iT}, \quad \bar{B}_{ij}^i = -\frac{|e_{ij}|}{R_{ij}}, \quad \bar{B}_{ij}^j = \frac{|e_{ij}|}{R_{ij}} \quad (12)$$

<sup>167</sup> where  $R_{ij}$  is the equivalent thermal resistance between two neighboring components  $\Omega_i$  and  
<sup>168</sup>  $\Omega_j$ , and  $R_i$  is the thermal resistance between component  $\Omega_i$  and the Dirichlet boundary.  
<sup>169</sup> The thermal resistances are computed based on the geometry and material properties of the  
<sup>170</sup> components; details regarding their computation are provided in Appendix A.

### <sup>171</sup> 2.3.2 Surface Velocity Model

<sup>172</sup> The displacement is assumed to be *one-dimensional* on the heated boundary  $\Gamma_q$ , i.e., the  
<sup>173</sup> surface recedes only in the direction of the applied load. For example, in Fig. ??, the surface  
<sup>174</sup> displacement on the heated boundary occurs only in the negative  $y$ -direction for the three  
<sup>175</sup> components exposed to the hypersonic boundary layer; the fourth component is the substrate  
<sup>176</sup> and does not ablate. Displacements along the  $x$  direction is small relative to displacements  
<sup>177</sup> in the  $y$  direction, and are thus neglected.

<sup>178</sup> For the  $i$ -th ablating component, the SVM considered in this work takes the form,

$$\dot{\mathbf{w}} = \Xi \bar{\mathbf{u}} - \tilde{\mathbf{f}} \quad (13)$$

<sup>179</sup> where  $\Xi = \text{diag}(\alpha_1, \dots, \alpha_{\tilde{N}})$  and  $\tilde{\mathbf{f}} = (\alpha_1 \bar{u}_{0,1}, \dots, \alpha_{\tilde{N}} \bar{u}_{0,\tilde{N}})^\top$ . The constants  $\alpha_i$  are small  
<sup>180</sup> material-dependent constants, determined from the B' table, and  $\bar{u}_{0,i}$  is the constant initial  
<sup>181</sup> temperature of the ablative component. The SVM provides a relation between the surface's  
<sup>182</sup> temperature and recession velocity, based on pre-computed B' tables for the material.

<sup>183</sup> **2.3.3 Coupled Reduced-Physics Model**

<sup>184</sup> The LCM and SVM are combined to define the RPM for predicting the thermo-ablative  
<sup>185</sup> response of the TPS under hypersonic boundary layers. Specifically, the RPM is defined as  
<sup>186</sup> the LCM as in eq. (9), where the *geometry- and temperature-dependent matrices*  $\bar{\mathbf{A}}$ ,  $\bar{\mathbf{B}}$ , and  
<sup>187</sup>  $\bar{\mathbf{f}}$  are updated at each time step based on the current temperature  $\bar{\mathbf{u}}$  and displacements  $\mathbf{w}$   
<sup>188</sup> provided by the SVM. The RPM is formally stated as,

$$\tilde{\mathbf{A}}(\mathbf{s})\dot{\mathbf{s}} = \tilde{\mathbf{B}}(\mathbf{s})\mathbf{s} + \tilde{\mathbf{F}}(t) \quad (14a)$$

$$\tilde{\mathbf{z}} = \mathbf{I}\mathbf{s} \quad (14b)$$

<sup>189</sup> where the state  $\mathbf{s} = [\bar{\mathbf{u}}, \mathbf{w}]^\top \in \mathbb{R}^{2N}$  includes the *average temperature* and *one-dimensional*  
<sup>190</sup> *surface displacements*; these are used in the observable outputs  $\mathbf{z} = [\bar{\mathbf{u}}, \mathbf{w}]^\top \in \mathbb{R}^{N+\tilde{N}}$ , where  
<sup>191</sup>  $\tilde{N}$  is the number of ablating components and  $\tilde{N} \leq N$ . The matrices are given as,

$$\tilde{\mathbf{A}}(\mathbf{s}) = \begin{bmatrix} \bar{\mathbf{A}}(\mathbf{s}) & \mathbf{0} \\ \mathbf{0} & \mathbf{I} \end{bmatrix}, \quad \tilde{\mathbf{B}}(\mathbf{s}) = \begin{bmatrix} \bar{\mathbf{B}}(\mathbf{s}) & \mathbf{0} \\ \Xi & \mathbf{0} \end{bmatrix}, \quad \tilde{\mathbf{F}}(t) = \begin{bmatrix} \bar{\mathbf{f}}(t) \\ -\tilde{\mathbf{f}} \end{bmatrix} \quad (15)$$

<sup>192</sup> In the matrices  $\tilde{\mathbf{A}}$  and  $\tilde{\mathbf{B}}$ , the surface displacements  $\mathbf{w}$  are used to define the dimensions for  
<sup>193</sup> the  $\Omega_i$  component used in eqs. (11b) and (12), thus effectively coupling the LCM and SVM.

<sup>194</sup> **2.4 Summary of Modeling Approaches**

<sup>195</sup> The FOM (i.e., FEM) and RPM (i.e., LCM with SVM) are two different but mathemati-  
<sup>196</sup> cally connected solution strategies. Particularly, the LCM in eq. (9) not only resembles the  
<sup>197</sup> functional form of the DG model in eq. (8), but can be viewed as a special case of the latter,  
<sup>198</sup> where the mesh partition is extremely coarse, and the trial and test functions are piece-wise  
<sup>199</sup> constants. This removes all spatial variations within each component, and neglects advection  
<sup>200</sup> effects due to mesh motion.

<sup>201</sup> For example, consider the case where each component  $\Omega_i$  is treated as one single element,  
<sup>202</sup> and each element employs one constant basis function  $\phi_i = 1$ . The element-wise DG model  
<sup>203</sup> in eq. (7) simplifies into a scalar ODE,

$$\mathbf{A}^{(i)} = \bar{A}_i, \quad \mathbf{C}^{(i)} = 0, \quad \mathbf{B}_{ij}^{(i)} = -\sigma|e_{ij}|, \quad \mathbf{B}_{ij}^{(j)} = \sigma|e_{ij}|, \quad \mathbf{f}_i = |e_{iq}|\bar{q}_i + \sigma|e_{iT}|\bar{T}_i \quad (16)$$

<sup>204</sup> Clearly, the LCM is a coarse zeroth-order DG model with the inverse of thermal resistance  
<sup>205</sup> chosen as the element-wise penalty factors. Or conversely, the DG model is a refined version  
<sup>206</sup> of LCM via *hp*-adaptation.

<sup>207</sup> The FOM and RPM represent two extremes in the modeling fidelity and computational  
<sup>208</sup> cost spectrum. On one hand, the FOM is the most accurate but computationally expensive  
<sup>209</sup> to evaluate due to the fine mesh discretizations for both the temperature and displacement  
<sup>210</sup> fields, leading to possibly millions of state variables. On the other hand, the RPM consid-  
<sup>211</sup> ers only the average temperature of the material, from which the one-dimensional surface  
<sup>212</sup> displacements are computed by integrating eq. (13). This considerably reduces the com-  
<sup>213</sup> putational cost, but sacrifices local temperature information that are critical to properly  
<sup>214</sup> capture higher-order effects due to mesh motion and thermal gradients within each compo-  
<sup>215</sup> nent. Thus, neither the FOM nor the RPM is an universal approach for real-world analysis,  
<sup>216</sup> design, and optimization tasks for ablating TPS, where thousands of high-fidelity model  
<sup>217</sup> evaluations may be necessary. This issue motivates the development of the PIROM, which

218 can achieve the fidelity of FOM at a computational cost close to the RPM, while maintaining  
219 the generalizability to model parameters.

## 220 3 Physics-Infused Reduced-Order Modeling

221 The formulation of PIROM for ablating TPS starts by connecting the FOM, i.e., the DG-  
222 FEM, and the RPM, i.e., the LCM, via a coarse-graining procedure. This procedure pin-  
223 points the missing dynamics in the LCM when compared to DG-FEM. Subsequently, the  
224 Mori-Zwanzig (MZ) formalism is employed to determine the model form for the missing dy-  
225 namics in PIROM. Lastly, the data-driven identification of the missing dynamics in PIROM  
226 is presented.

### 227 3.1 Deriving the Reduced-Physics Model via Coarse-Graining

228 The subsequent coarse-graining formulation is performed on the DG-FEM in eq. (8) to derive  
229 the LCM in eq. (9). This process constraints the trial function space of a full-order DG model  
230 to a subset of piece-wise constants, so that the variables  $\mathbf{u}$ , matrices  $\mathbf{A}$ ,  $\mathbf{B}$ , and  $\mathbf{C}$ , and forcing  
231 vector  $\mathbf{f}$  are all approximated using a single state associated to the average temperature.  
232 Note that the coarse-graining is exclusively performed on the thermal dynamics, as it is  
233 the surface temperature that drives the one-dimensional recession via the SVM. Hence, the  
234 coarse-graining of the mesh dynamics is not included in the following procedure.

#### 235 3.1.1 Coarse-Graining of States

236 Consider a DG model as in eq. (8) for  $M$  elements and an LCM as in eq. (9) for  $N$  components;  
237 clearly  $M \gg N$ . Let  $\mathcal{V}_j = \{i | E_i \in \Omega_j\}$  be the indices of the elements belonging to the  $j$ -th  
238 component, so  $E_i \in \Omega_j$  for all  $i \in \mathcal{V}_j$ . The number of elements in the  $j$ -th component is  $|\mathcal{V}_j|$ .

<sup>239</sup> The average temperature on  $\Omega_j$  is,

$$\bar{u}_j = \frac{1}{|\Omega_j|} \sum_{i \in \mathcal{V}_j} \int_{E^{(i)}} \boldsymbol{\phi}^{(i)}(x)^T \mathbf{u}^{(i)} d\Omega = \frac{1}{|\Omega_j|} \sum_{i \in \mathcal{V}_j} |E_i| \boldsymbol{\varphi}_i^{j\top} \mathbf{u}^{(i)}, \quad j = 1, 2, \dots, N \quad (17)$$

<sup>240</sup> where  $|\Omega_j|$  and  $|E_i|$  denote the area ( $d = 2$ ) or volume ( $d = 3$ ) of component  $j$  and element <sup>241</sup>  $i$ , respectively. The orthogonal basis functions are defined as  $\boldsymbol{\varphi}_i^{j\top} = [1, 0, \dots, 0]^\top \in \mathbb{R}^P$ .

<sup>242</sup> Conversely, given the average temperatures of the  $N$  components,  $\bar{\mathbf{u}}$ , the states of an <sup>243</sup> arbitrary element  $E_i$  is written as,

$$\mathbf{u}^{(i)} = \sum_{k=1}^N \boldsymbol{\varphi}_i^k \bar{u}_k + \delta \mathbf{u}^{(i)}, \quad i = 1, 2, \dots, M \quad (18)$$

<sup>244</sup> where  $\boldsymbol{\varphi}_i^k = 0$  if  $i \notin \mathcal{V}_k$ , and  $\delta \mathbf{u}^{(i)}$  represents the deviation from the average temperature and <sup>245</sup> satisfies the orthogonality condition  $\boldsymbol{\varphi}_i^k \delta \mathbf{u}^{(i)} = 0$  for all  $k$ .

<sup>246</sup> Equations eqs. (17) and (18) are combined and written in matrix form as,

$$\bar{\mathbf{u}} = \boldsymbol{\Phi}^+ \mathbf{u}, \quad \mathbf{u} = \boldsymbol{\Phi} \mathbf{u} + \delta \mathbf{u} \quad (19)$$

<sup>247</sup> where  $\boldsymbol{\Phi} \in \mathbb{R}^{MP \times N}$  is a matrix of  $M \times N$  blocks, with the  $(i, j)$ -th block as  $\boldsymbol{\varphi}_i^j$ ,  $\boldsymbol{\Phi}^+ \in \mathbb{R}^{N \times MP}$  <sup>248</sup> is the left inverse of  $\boldsymbol{\Phi}$ , with the  $(i, j)$ -th block as  $\boldsymbol{\varphi}_i^{j+} = \frac{|E_i|}{|\Omega_j|} \boldsymbol{\varphi}_i^{j\top}$ , and  $\delta \mathbf{u}$  is the collection of <sup>249</sup> deviations. By their definitions,  $\boldsymbol{\Phi}^+ \boldsymbol{\Phi} = \mathbf{I}$  and  $\boldsymbol{\Phi}^+ \delta \mathbf{u} = \mathbf{0}$ .

### <sup>250</sup> 3.1.2 Coarse-Graining of Dynamics

<sup>251</sup> The dependence of the matrices with respect to the displacements  $\mathbf{w}$  is dropped to isolate <sup>252</sup> the analysis based on coarsened variables. Consider a function of states in the form of <sup>253</sup>  $\mathbf{M}(\mathbf{u}) \mathbf{g}(\mathbf{u})$ , where  $\mathbf{g} : \mathbb{R}^{MP} \rightarrow \mathbb{R}^{MP}$  is a vector-valued function, and  $\mathbf{M} : \mathbb{R}^{MP} \rightarrow \mathbb{R}^{p \times MP}$  <sup>254</sup> is a matrix-valued function with an arbitrary dimension  $p$ . Define the projection matrix

255  $\mathbf{P} = \Phi\Phi^+$  and the projection operator  $\mathcal{P}$  as,

$$\begin{aligned}\mathcal{P}[\mathbf{M}(\mathbf{u})\mathbf{g}(\mathbf{u})] &= \mathbf{M}(\mathbf{P}\mathbf{u})\mathbf{g}(\mathbf{P}\mathbf{u}) \\ &= \mathbf{M}(\Phi\bar{\mathbf{u}})\mathbf{g}(\Phi\bar{\mathbf{u}})\end{aligned}\quad (20)$$

256 so that the resulting function depends only on the average temperatures  $\bar{\mathbf{u}}$ . Correspondingly,  
257 the residual operator  $\mathcal{Q} = \mathcal{I} - \mathcal{P}$ , and  $\mathcal{Q}[\mathbf{M}(\mathbf{u})\mathbf{g}(\mathbf{u})] = \mathbf{M}(\mathbf{u})\mathbf{g}(\mathbf{u}) - \mathbf{M}(\Phi\bar{\mathbf{u}})\mathbf{g}(\Phi\bar{\mathbf{u}})$ . When  
258 the function is not separable, the projection operator is simply defined as  $\mathcal{P}[\mathbf{g}(\mathbf{u})] = \mathbf{g}(\mathbf{P}\mathbf{u})$ .

259 Subsequently, the operators defined above are applied to coarse-grain the dynamics. First,  
260 write the DG-FEM in eq. (8) as,

$$\dot{\mathbf{u}} = \mathbf{A}(\mathbf{u})^{-1}\mathbf{B}(\mathbf{u})\mathbf{u} + \mathbf{A}(\mathbf{u})^{-1}\mathbf{C}(\mathbf{u})\mathbf{u} + \mathbf{A}(\mathbf{u})^{-1}\mathbf{f}(t) \quad (21)$$

261 and multiply both sides by  $\Phi^+$  to obtain,

$$\Phi^+\dot{\mathbf{u}} = \Phi^+(\Phi\dot{\bar{\mathbf{u}}} + \delta\dot{\mathbf{u}}) = \dot{\bar{\mathbf{u}}} = \Phi^+\mathbf{r}(\mathbf{u}, t) \quad (22)$$

262 Apply the projection operator  $\mathcal{P}$  and the residual operator  $\mathcal{Q}$  to the right-hand side to obtain,

$$\dot{\bar{\mathbf{u}}} = \mathcal{P}[\Phi^+\mathbf{r}(\mathbf{u}, t)] + \mathcal{Q}[\Phi^+\mathbf{r}(\mathbf{u}, t)] \equiv \mathbf{r}^{(1)}(\mathbf{u}, t) + \mathbf{r}^{(2)}(\mathbf{u}, t) \quad (23)$$

263 where  $\mathbf{r}^{(1)}(\mathbf{u}, t)$  is resolved dynamics that depends on  $\bar{\mathbf{u}}$  only, and  $\mathbf{r}^{(2)}(\mathbf{u}, t)$  is the un-resolved  
264 or residual dynamics. Detailed derivations and analysis of  $\mathbf{r}^{(1)}(\mathbf{u}, t)$  and  $\mathbf{r}^{(2)}(\mathbf{u}, t)$  can be  
265 found in the Appendix.

266 It follows from Ref. [12] that the resolved dynamics is exactly the LCM, where the  
267 advection term reduces to zero, i.e.,  $\bar{\mathbf{C}}(\bar{\mathbf{u}}) = \mathbf{0}$  as shown in the Appendix. Using the notation

268 from eq. (9), it follows that,

$$\begin{aligned}\mathbf{r}^{(1)}(\mathbf{u}, t) &= \bar{\mathbf{A}}(\bar{\mathbf{u}})^{-1}\bar{\mathbf{B}}(\bar{\mathbf{u}})\bar{\mathbf{u}} + \bar{\mathbf{A}}(\bar{\mathbf{u}})^{-1}\bar{\mathbf{C}}(\bar{\mathbf{u}})\bar{\mathbf{u}} + \bar{\mathbf{A}}(\bar{\mathbf{u}})^{-1}\bar{\mathbf{f}}(\bar{\mathbf{u}}) \\ &= \bar{\mathbf{A}}(\bar{\mathbf{u}})^{-1}\bar{\mathbf{B}}(\bar{\mathbf{u}})\bar{\mathbf{u}} + \bar{\mathbf{A}}(\bar{\mathbf{u}})^{-1}\bar{\mathbf{f}}(t)\end{aligned}\quad (24)$$

269 where the following relations hold,

$$\bar{\mathbf{A}}(\bar{\mathbf{u}}) = \mathbf{W} (\Phi^+ \mathbf{A} (\Phi \bar{\mathbf{u}})^{-1} \Phi)^{-1} \quad \bar{\mathbf{C}}(\bar{\mathbf{u}}) = \mathbf{0} \quad (25a)$$

$$\bar{\mathbf{B}}(\bar{\mathbf{u}}) = \mathbf{W} \Phi^+ \mathbf{B} (\Phi \bar{\mathbf{u}}) \Phi \quad \bar{\mathbf{f}}(t) = \mathbf{W} \Phi^+ \mathbf{f} \quad (25b)$$

270 where  $\mathbf{W} \in \mathbb{R}^{N \times N}$  is a diagonal matrix with the  $i$ -th element as  $[\mathbf{W}]_{ii} = |\mathcal{V}_k|$  if  $i \in \mathcal{V}_k$ .

271 The examination of the second residual term  $\mathbf{r}^{(2)}(\mathbf{u}, t)$  in eq. (23) is shown in the Appendix,  
272 and demonstrates that the physical sources of missing dynamics in the LCM include: the  
273 approximation of non-uniform temperature within each component as a constant, and the  
274 elimination of the advection term due to coarse-graining. In sum, the above results not  
275 only show that the LCM is a result of coarse-graining of the full-order DG-FEM, but also  
276 reveal the discrepancies between the LCM and the DG-FEM. These discrepancies propagate  
277 into the SVM, which as a result of the averaging in the LCM formulation, under-predicts  
278 the surface recession rates. In the subsequent section, the discrepancies in the LCM are  
279 corrected to formulate the PIROM.

### 280 3.2 Physics-Infusion Via Mori-Zwanzig Formalism

281 The Mori-Zwanzig (MZ) formalism is an operator-projection technique used to derive ROMs  
282 for high-dimensional dynamical systems, especially in statistical mechanics and fluid dynam-  
283 ics [9, 10, 11]. It provides an exact reformulation of a high-dimensional Markovian dynamical  
284 system, into a low-dimensional observable non-Markovian dynamical system. The proposed  
285 ROM is subsequently developed based on the approximation to the non-Markovian term in

the observable dynamics. Particularly, eq. (23) shows that the DG-FEM dynamics can be decomposed into the resolved dynamics  $\mathbf{r}^{(1)}(\mathbf{u}, t)$  and the orthogonal dynamics  $\mathbf{r}^{(2)}(\mathbf{u}, t)$ , in the sense of  $\mathcal{P}\mathbf{r}^{(2)} = 0$ . In this case, the MZ formalism can be invoked to express the dynamics  $\bar{\mathbf{u}}$  in terms of  $\bar{\mathbf{u}}$  alone as the projected Generalized Langevin Equation (GLE) [9, 10, 11],

$$\dot{\bar{\mathbf{u}}}(t) = \mathbf{r}^{(1)}(\bar{\mathbf{u}}, t) + \int_0^t \tilde{\kappa}(t, s, \bar{\mathbf{u}}) ds \quad (26)$$

where the first and second terms are referred to as the Markovian and non-Markovian terms, respectively. The non-Markovian term accounts for the effects of past un-resolved states on the current resolved states via a memory kernel  $\tilde{\kappa}(t, s, \bar{\mathbf{u}})$ , which in practice is computationally expensive to evaluate.

### 3.2.1 Markovian Reformulation

This section details the formal derivation of the PIROM as a system of ODEs for the thermal dynamics, based on approximations to the memory kernel. Specifically, the kernel  $\tilde{\kappa}$  is examined via a leading-order expansion, based on prior work [13]; this can be viewed as an analog of zeroth-order holding in linear system theory with a sufficiently small time step. In this case, the memory kernel is approximated as,

$$\tilde{\kappa}(t, s, \bar{\mathbf{u}}) \approx \mathbf{r}^{(1)}(\bar{\mathbf{u}}, t) \cdot \nabla_{\bar{\mathbf{u}}} \mathbf{r}^{(2)}(\Phi \bar{\mathbf{u}}, t) \quad (27)$$

Note that the terms in  $\mathbf{r}^{(1)}$  have a common factor  $\bar{\mathbf{A}}^{-1}$ ; this motivates the following heuristic modification of the model form in eq. (26),

$$\dot{\bar{\mathbf{u}}} = \mathbf{r}^{(1)}(\bar{\mathbf{u}}, t) + \bar{\mathbf{A}}^{-1}(\bar{\mathbf{u}}) \int_0^t \kappa(t, s, \bar{\mathbf{u}}) ds \quad (28a)$$

$$\bar{\mathbf{A}}(\bar{\mathbf{u}}) \dot{\bar{\mathbf{u}}} = \bar{\mathbf{B}}(\bar{\mathbf{u}}) \bar{\mathbf{u}} + \bar{\mathbf{f}}(t) + \int_0^t \kappa(t, s, \bar{\mathbf{u}}) ds \quad (28b)$$

302 where the original kernel  $\tilde{\kappa}$  is effectively normalized by  $\bar{\mathbf{A}}^{-1}$ . Intuitively, such choice of kernel  
 303 reduces its dependency on the averaged material properties, and simplifies the subsequent  
 304 design of model form.

305 Subsequently, the hidden states are introduced to “Markovianize” the system eq. (26).  
 306 In this manner, eq. (28b) is converted into a pure state-space model, with the functional  
 307 form of the LCM retained; since LCM is a physics-based model, then it encodes the phys-  
 308 ical information and retains explicit parametric dependence of the problem. Consider the  
 309 representation of the kernel as a finite sum of simpler functions, e.g., exponentials,

$$\kappa(t, s, \bar{\mathbf{u}}) = \sum_{j=1}^m \mathcal{K}_j(t, s, \bar{\mathbf{u}}) [\mathbf{p}_j + \mathbf{d}_j(\bar{\mathbf{u}})] \phi_j(s, \bar{\mathbf{u}}) \quad (29)$$

310 where,

$$\mathcal{K}_j(t, s, \bar{\mathbf{u}}) = e^{-\int_s^t (\lambda_j + e_j(\bar{\mathbf{u}})) d\tau}, \quad \phi_j(s, \bar{\mathbf{u}}) = \mathbf{q}_j^\top \bar{\mathbf{u}}(s) + \mathbf{g}_j(\bar{\mathbf{u}})^\top \bar{\mathbf{u}}(s) + \mathbf{r}_j^\top \bar{\mathbf{f}}(s) \quad (30)$$

311 with suitable coefficients  $\mathbf{p}_j, \mathbf{d}_j, \mathbf{q}_j, \mathbf{g}_j, \mathbf{r}_j \in \mathbb{R}^N$  and decay rates  $\lambda_j, e_j(\bar{\mathbf{u}}) > 0$ , that need to  
 312 be identified from data.

313 Define the hidden states as,

$$\beta_j(t) = \int_0^t \mathcal{K}_j(s, \bar{\mathbf{u}}) \phi_j(s, \bar{\mathbf{u}}) ds \quad (31)$$

314 and differentiate with respect to time,,

$$\dot{\beta}_j(t) = -[\lambda_j + e_j(\bar{\mathbf{u}})] \beta_j(t) + \mathbf{q}_j^\top \bar{\mathbf{u}}(t) + \mathbf{g}_j(\bar{\mathbf{u}})^\top \bar{\mathbf{u}}(t) + \mathbf{r}_j^\top \bar{\mathbf{f}}(t) \quad (32)$$

315 to obtain the memory,

$$\int_0^t \kappa(t, s, \bar{\mathbf{u}}) ds = \sum_{j=1}^m [\mathbf{p}_j + \mathbf{d}_j(\bar{\mathbf{u}})] \beta_j(t) \quad (33)$$

<sup>316</sup> Then, eq. (28b) is recast as the extended Markovian system,

$$\bar{\mathbf{A}}(\bar{\mathbf{u}})\dot{\bar{\mathbf{u}}} = \bar{\mathbf{B}}(\bar{\mathbf{u}})\bar{\mathbf{u}} + [\mathbf{P} + \mathbf{D}(\bar{\mathbf{u}})]\boldsymbol{\beta} + \bar{\mathbf{f}}(t) \quad (34a)$$

$$\dot{\boldsymbol{\beta}} = [\mathbf{Q} + \mathbf{G}(\bar{\mathbf{u}})]\bar{\mathbf{u}} + [\mathbf{E}(\bar{\mathbf{u}}) - \boldsymbol{\Lambda}]\boldsymbol{\beta} + \mathbf{R}\bar{\mathbf{f}}(t) \quad (34b)$$

<sup>317</sup> where the data-driven operators associated to the hidden dynamics are collected as,

$$\boldsymbol{\Lambda} = \text{diag}(\lambda_1, \lambda_2, \dots, \lambda_m) \in \mathbb{R}^{m \times m}, \quad \mathbf{P} = [\mathbf{p}_1, \mathbf{p}_2, \dots, \mathbf{p}_m] \in \mathbb{R}^{N \times m} \quad (35a)$$

$$\mathbf{D}(\bar{\mathbf{u}}) = [\mathbf{d}_1(\bar{\mathbf{u}}), \mathbf{d}_2(\bar{\mathbf{u}}), \dots, \mathbf{d}_m(\bar{\mathbf{u}})] \in \mathbb{R}^{N \times m}, \quad \mathbf{Q} = [\mathbf{q}_1, \mathbf{q}_2, \dots, \mathbf{q}_m] \in \mathbb{R}^{m \times N} \quad (35b)$$

$$\mathbf{G}(\bar{\mathbf{u}}) = [\mathbf{g}_1(\bar{\mathbf{u}}), \mathbf{g}_2(\bar{\mathbf{u}}), \dots, \mathbf{g}_m(\bar{\mathbf{u}})] \in \mathbb{R}^{m \times N}, \quad \mathbf{R} = [\mathbf{r}_1, \mathbf{r}_2, \dots, \mathbf{r}_m] \in \mathbb{R}^{m \times N} \quad (35c)$$

$$\mathbf{E}(\bar{\mathbf{u}}) = \text{diag}(e_1(\bar{\mathbf{u}}), e_2(\bar{\mathbf{u}}), \dots, e_m(\bar{\mathbf{u}})) \in \mathbb{R}^{m \times m} \quad (35d)$$

<sup>318</sup> The form of the temperature-dependent matrices  $\mathbf{D}(\bar{\mathbf{u}})$ ,  $\mathbf{G}(\bar{\mathbf{u}})$ , and  $\mathbf{E}(\bar{\mathbf{u}})$  is specified in the  
<sup>319</sup> next section. Since the hidden states  $\boldsymbol{\beta}$  serve as the memory, their initial conditions are set  
<sup>320</sup> to zero, i.e.,  $\boldsymbol{\beta}(t_0) = \mathbf{0}$ , no memory at the beginning. The physics-infused model in eq. (34b)  
<sup>321</sup> retains the structure of the LCM, while the hidden states account for missing physics through  
<sup>322</sup> corrections to the stiffness and advection matrices, as well as the forcing term.

### <sup>323</sup> 3.2.2 Coupled Physics-Infused Model

<sup>324</sup> The next step involves coupling the physics-infused model in eq. (34b) with the SVM in  
<sup>325</sup> eq. (13) to define the PIROM for ablating TPS. To this end, define the observables as the  
<sup>326</sup> surface temperature  $\mathbf{z}_u \in \mathbb{R}^{\tilde{N}}$  and displacements  $\mathbf{z}_w \in \mathbb{R}^{\tilde{N}}$  for  $\tilde{N} \leq N$  ablating components  
<sup>327</sup> to define the observable vector as  $\mathbf{z} = [\mathbf{z}_u, \mathbf{z}_w]^\top \in \mathbb{R}^{n_z}$  with  $n_z = 2\tilde{N}$  as the total number of  
<sup>328</sup> observables.

<sup>329</sup> Collect the RPM and hidden states into a single state vector  $\mathbf{y} = [\bar{\mathbf{u}}, \mathbf{w}, \boldsymbol{\beta}]^\top \in \mathbb{R}^{n_y}$ , where  
<sup>330</sup>  $n_y = N + \tilde{N} + m$ , and define a data-driven operator  $\mathbf{M} \in \mathbb{R}^{n_z \times n_y}$  to define the PIROM's

<sup>331</sup> observable as,

$$\mathbf{z} = \mathbf{M}\mathbf{y} \quad (36)$$

<sup>332</sup> where,

$$\mathbf{M} = \begin{bmatrix} \mathbf{M}_{\bar{u}} & \mathbf{0} & \mathbf{M}_{\beta} \\ \mathbf{0} & \mathbf{I} & \mathbf{0} \end{bmatrix} \quad (37)$$

<sup>333</sup> includes the matrices  $\mathbf{M}_{\bar{u}} \in \mathbb{R}^{\tilde{N} \times N}$  and  $\mathbf{M}_{\beta} \in \mathbb{R}^{\tilde{N} \times m}$ , which computes the surface temperature observable from the RPM states and hidden states, respectively. The PIROM is coupled  
<sup>334</sup> to the SVM in eq. (13) by leveraging eq. (36) to compute the surface recession velocity. Thus,  
<sup>335</sup> the PIROM is formally stated as,

$$\mathcal{A}\dot{\mathbf{y}} = [\mathcal{B} + \mathcal{C}]\mathbf{y} + \mathcal{F}(t) \quad (38a)$$

$$\mathbf{z} = \mathbf{M}\mathbf{y} \quad (38b)$$

<sup>337</sup> where,

$$\mathcal{A} = \begin{bmatrix} \bar{\mathbf{A}} & \mathbf{O} & \mathbf{O} \\ \mathbf{O} & \mathbf{I} & \mathbf{O} \\ \mathbf{O} & \mathbf{O} & \mathbf{I} \end{bmatrix} \in \mathbb{R}^{n_y \times n_y}, \quad \mathcal{B} = \begin{bmatrix} \bar{\mathbf{B}} & \mathbf{O} & \mathbf{P} \\ \Xi\mathbf{M}_u & \mathbf{O} & \Xi\mathbf{M}_{\beta} \\ \mathbf{Q} & \mathbf{O} & -\Lambda \end{bmatrix} \in \mathbb{R}^{n_y \times n_y}, \quad (39a)$$

$$\mathcal{C} = \begin{bmatrix} \mathbf{O} & \mathbf{O} & \mathbf{D}(\bar{\mathbf{u}}) \\ \mathbf{O} & \mathbf{O} & \mathbf{O} \\ \mathbf{G}(\bar{\mathbf{u}}) & \mathbf{O} & \mathbf{E}(\bar{\mathbf{u}}) \end{bmatrix} \in \mathbb{R}^{n_y \times n_y}, \quad \mathcal{F} = \begin{bmatrix} \bar{\mathbf{f}}(t) \\ -\tilde{\mathbf{f}} \\ \mathbf{R}\bar{\mathbf{f}}(t) \end{bmatrix} \in \mathbb{R}^{n_y} \quad (39b)$$

<sup>338</sup> The learnable parameters in the PIROM are collected as,

$$\Theta = \{\mathbf{P}, \mathbf{Q}, \mathbf{R}, \mathbf{D}(\bar{\mathbf{u}}), \mathbf{G}(\bar{\mathbf{u}}), \mathbf{E}(\bar{\mathbf{u}}), \mathbf{M}_u, \mathbf{M}_{\beta}\}, \in \mathbb{R}^{n_{\theta}} \quad (40)$$

<sup>339</sup> Particularly, the matrices  $\mathbf{P}, \mathbf{A}, \mathbf{Q}, \mathbf{R}$  are constants that need to be identified from data, and  
<sup>340</sup> account for the effects of coarse-graining on the stiffness and forcing matrices. The matrices

<sup>341</sup>  $\mathbf{D}(\bar{\mathbf{u}})$ ,  $\mathbf{E}(\bar{\mathbf{u}})$ ,  $\mathbf{G}(\bar{\mathbf{u}})$  are state-dependent matrices, and account for the effects of coarse-graining  
<sup>342</sup> on the advection matrix due to mesh motion. Leveraging the DG-FEM formula for the  
<sup>343</sup> advection matrix in eq. (55c) in the Appendix, and noting that the ablating velocity in  
<sup>344</sup> eq. (4) imposes the boundary condition for the mesh motion, the state-dependent matrices  
<sup>345</sup> for the  $i$ -th component are written as,

$$\mathbf{D}(\bar{\mathbf{u}}) \approx \dot{\mathbf{w}}(\bar{\mathbf{u}}) \odot_r \mathbf{D}, \quad \mathbf{G}(\bar{\mathbf{u}}) \approx \mathbf{G} \odot_r \dot{\mathbf{w}}(\bar{\mathbf{u}}), \quad \mathbf{E}(\bar{\mathbf{u}}) \approx \dot{\mathbf{W}}(\bar{\mathbf{u}}) \odot \mathbf{E} \quad (41)$$

<sup>346</sup> where  $\dot{\mathbf{w}}(\bar{\mathbf{u}})$  is the SVM based on the observable temperature  $\bar{\mathbf{u}}$ ,  $\odot_r$  is the row-wise multipli-  
<sup>347</sup> cation, and  $\dot{\mathbf{W}}$  is the concatenation of  $\dot{\mathbf{w}}$  for  $\tilde{m}$  times, where  $\tilde{m}$  corresponds to the number  
<sup>348</sup> of hidden states per component, i.e.,  $m = N\tilde{m}$ .

<sup>349</sup> The PIROM in eq. (38b) incorporates explicit information on the material properties,  
<sup>350</sup> boundary conditions, and surface recession, and is designed to generalize across parametric  
<sup>351</sup> variations in these inputs. Moreover, the hidden dynamics in eq. (34b) are interpretable,  
<sup>352</sup> as these retain the functional form of the DG-FEM in eq. (8). The next step is focused on  
<sup>353</sup> identifying the unknown data-driven parameters  $\Theta$  characterizing the hidden dynamics.

### <sup>354</sup> 3.3 Learning the Hidden Dynamics

<sup>355</sup> Learning of the PIROM is achieved through a gradient-based neural-ODE-like approach [3].  
<sup>356</sup> For ease of presentation, consider the compact form of the PIROM in eq. (38b),

$$\mathcal{D}(\dot{\mathbf{y}}, \mathbf{y}, \boldsymbol{\xi}, \mathcal{F}; \Theta) = \mathbf{0} \quad (42)$$

<sup>357</sup> where  $\boldsymbol{\xi}$  defines the model parameters, i.e., material properties and B' tables, while  $\mathcal{F}$   
<sup>358</sup> represents the forcing terms, i.e., the boundary conditions.

<sup>359</sup> Consider a dataset of  $N_s$  high-fidelity *surface temperature* observable trajectories  $\mathbf{z}_{HF}$ ,  
<sup>360</sup> sampled at  $p$  time instances  $\{t_k\}_{k=0}^{p-1}$ , for different parameter settings  $\{\boldsymbol{\xi}^{(l)}\}_{l=1}^{N_s}$  and forcing

<sup>361</sup> functions  $\{\mathcal{F}^{(l)}(t)\}_{l=1}^{N_s}$ . The dataset is expressed as,

$$\mathcal{D} = \left\{ \left( t_k, \mathbf{z}_{\text{HF}}^{(l)}(t_k), \boldsymbol{\xi}^{(l)}, \mathcal{F}^{(l)}(t_k) \right) \right\}_{l=1}^{N_s}, \quad k = 0, 1, \dots, p-1 \quad (43)$$

<sup>362</sup> In this work, the dataset contains only surface temperature observables – all high-fidelity  
<sup>363</sup> information regarding the surface displacements *are assumed to be unavailable during learn-*  
<sup>364</sup> *ing.*

<sup>365</sup> The learning problem is formulated as the following differentially-constrained problem,

$$\min_{\Theta} \quad \mathcal{J}(\Theta; \mathcal{D}) = \sum_{l=1}^{N_s} \int_{t_0}^{t_f} \ell \left( \mathbf{z}_u^{(l)}, \mathbf{z}_{\text{HF}}^{(l)} \right) dt \quad (44a)$$

$$\text{s.t.} \quad \mathbf{0} = \mathcal{D} \left( \dot{\mathbf{y}}^{(l)}, \mathbf{y}^{(l)}, \boldsymbol{\xi}^{(l)}, \mathcal{F}^{(l)}; \Theta \right) \quad (44b)$$

<sup>366</sup> for  $l = 1, 2, \dots, N_s$ , the objective is to minimize the discrepancy between the high-fidelity  
<sup>367</sup> and PIROM predictions for the  $l$ -th trajectory with  $\ell \left( \mathbf{z}_u^{(l)}, \mathbf{z}_{\text{HF}}^{(l)} \right) = \left\| \mathbf{z}_u^{(l)} - \mathbf{z}_{\text{HF}}^{(l)} \right\|_2^2$ .

<sup>368</sup> The gradient-based optimization loop is based on the adjoint variable  $\boldsymbol{\lambda}$ , governed by the  
<sup>369</sup> adjoint differential equation,

$$\frac{\partial \ell}{\partial \mathbf{y}} + \boldsymbol{\lambda}^\top \frac{\partial \mathcal{D}}{\partial \mathbf{y}} - \frac{d}{dt} \left( \boldsymbol{\lambda}^\top \frac{\partial \mathcal{D}}{\partial \dot{\mathbf{y}}} \right) = \mathbf{0} \quad (45a)$$

$$\boldsymbol{\lambda}(t_f)^\top \frac{\partial \mathcal{D}}{\partial \dot{\mathbf{y}}(t_f)} = \mathbf{0} \quad (45b)$$

<sup>370</sup> Once  $\boldsymbol{\lambda}$  is solved, the gradient is computed as,

$$\nabla_{\Theta} \mathcal{J} = \frac{1}{N_s} \sum_{l=1}^{N_s} \int_{t_0}^{t_f} \left( \frac{\partial \ell}{\partial \Theta} + (\boldsymbol{\lambda}^{(l)})^\top \frac{\partial \mathcal{D}}{\partial \Theta} \right) dt \quad (46)$$

<sup>371</sup>

Discussion on TSA?

## 372 4 Application to Thermal Protection Systems

373 In this section, the proposed PIROM approach is applied to the analysis of thermo-ablative  
374 multi-layered hypersonic TPS. The performance of the PIROM is evaluated in terms of  
375 *accuracy, generalizability, and computational efficiency*, across a range of boundary condition  
376 and surface velocity model parametrizations. The results show PIROM to be a promising  
377 candidate for the solution of the impossible trinity of modeling.

### 378 4.1 Problem Definition

379 Consider the two-dimensional TPS configuration shown in Fig. x with constant material  
380 properties within each layer, dimensions, and BCs listed in Table x. Such configuration is  
381 representative of the TPS used for the initial concept 3.X vehicle in past studies [8], and in-  
382 volves two main layers: an outer ablative layer, and an inner substrate layer. The top ablative  
383 layer may be composed of different materials, such as PICA or Avcoat, while the substrate  
384 layer is typically made of a high-temperature resistant material, such as carbon-carbon com-  
385 posite [6]. The ablative layer, composed of  $\tilde{N} = 3$  ablative components, is subjected to  
386 strong time-varying and non-uniform heating, while the substrate layer, composed of one  
387 non-ablative component, is insulated adiabatically at the outer surface; the total number of  
388 components is thus  $N = 4$ .

389 The lumped-mass representation of the TPS configuration is shown in Fig. 2, where each  
390 component  $\Omega_i$  is represented by a lumped mass with uniform temperature  $u_i(t)$ . Details  
391 regarding the derivation of the LCM for this configuration are provided in Appendix A.  
392 The sources of non-linearities studied in this problem originate from the coupling between  
393 the thermodynamics and temperature-dependent mesh motion, i.e., geometry-dependent  
394 matrices, as well as the heterogeneities across material layers. As shown in Fig. x, perfect  
395 thermocouple devices are placed at the surfaces of the ablative layers for the collection of  
396 the high-fidelity temperature signals that are used in the following sections for training and

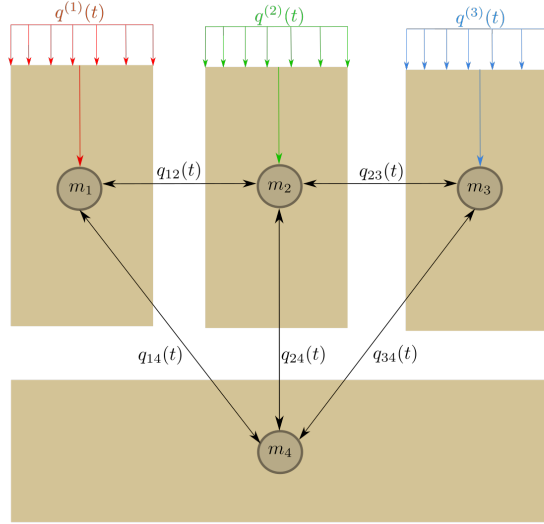


Figure 2: Lumped-mass representation of the multi-layered TPS configuration considered in this work.

<sup>397</sup> testing the PIROM.

## <sup>398</sup> 4.2 Parametrization of Boundary Conditions and Surface Velocity <sup>399</sup> Models

<sup>400</sup> The operating conditions of the TPS are specified by the boundary conditions, i.e., the heat  
<sup>401</sup> flux, and the surface velocity model (SVM). Specifically, the heat flux on the Neumann  
<sup>402</sup> BC is parametrized using  $\xi_{\text{BC}} = \{\xi_0, \xi_1, \xi_2\}$ , while the SVM is parametrized using  $\xi_{\text{SVM}} =$   
<sup>403</sup>  $\{\alpha_1, \alpha_2, \alpha_3\}$ . Thus, the heat flux and SVM over the  $i$ -th ablative component are expressed  
<sup>404</sup> as,

$$q(x, t; \xi_{\text{BC}}) = \xi_0 e^{\xi_1 x} e^{\xi_2 t}, \forall x \in \Gamma_{i,q}, \quad \dot{w}_i(z_{u,i}; \xi_{\text{SVM}}) = \alpha_i (z_{u,i} - u_{0,i}) \quad (47)$$

<sup>405</sup> where  $\Gamma_{i,q}$ ,  $z_{u,i}$ , and  $u_{0,i}$  correspond to the Neumann BC surface, the PIROM's surface tem-  
<sup>406</sup> perature prediction, and the initial temperature of the  $i$ -th ablative component, respectively.

<sup>407</sup> The  $\xi_0$  controls the magnitude of the heat flux, while  $\xi_1$  and  $\xi_2$  control the spatial and  
<sup>408</sup> temporal variations, respectively. The constant  $\alpha_i$  is a small material-dependent constant  
<sup>409</sup> determined from the B' table, specifying the ablation velocity for a given change in surface

410 temperature.

### 411 4.3 Data Generation

412 Full-order solutions of the TPS are computed using the FEM multi-mechanics module of  
413 the **Aria** package [4], where the mesh is shown in Fig. x. The mesh consists of 2196  
414 total elements, with 366 elements for each ablative component and 1098 elements for the  
415 substrate component. All solutions are computed for one minute from an uniform initial  
416 temperature of  $T(x, t_0) = 300$  K. Given an operating condition  $\xi = [\xi_{\text{BC}}, \xi_{\text{SVM}}]^{\top}$ , a full-  
417 order solution consists of then collection of time-varying temperature and displacement fields  
418  $\left\{ \left( t_k, \mathbf{u}_{\text{HF}}^{(l)}(t_k), \mathbf{w}_{\text{HF}}^{(l)}(t_k), \xi^{(l)} \right) \right\}_{k=0}^{p-1}$ , where  $p$  is the number of time steps with a step size of  
419  $\Delta t \approx 10^{-3}$ . The observable trajectories are representative of near-wall thermocouple sensing  
420 of hypersonic flows involving heat transfer. At each time instance  $t_k$ , a temperature reading is  
421 recorded from each ablative component using the thermocouples shown in Fig. x, resulting  
422 in three temperature signals, i.e., the observables  $\mathbf{z}_{\text{HF}} \in \mathbb{R}^3$ . Therefore, each full-order  
423 solution produces one trajectory of observables  $\left\{ \left( t_k, \mathbf{z}_{\text{HF}}^{(l)}(t_k), \xi^{(l)} \right) \right\}_{k=0}^{p-1}$ . The goal of the  
424 PIROM is to predict the surface temperature and displacement as accurately as possible.

#### 425 4.3.1 Definition of Training and Testing Datasets

426 The range of parameters used to generate the training  $\mathcal{D}_1$  and testing  $\{\mathcal{D}_2, \mathcal{D}_3\}$  datasets  
427 are listed in Table x. The training and testing datasets are designed, respectively, to: (1)  
428 minimize the information that the PIROM can “see”, and (2) to maximize the variabil-  
429 ity of test operating conditions to examine the PIROM’s generalization performance. A  
430 total of 110 normally-distributed data points for the BC parametrization are visualized in  
431 Fig. 3(a), and the corresponding observable trajectories are shown in Figs. 3(b) and 3(c).  
432 The training dataset  $\mathcal{D}_1$  includes 10 trajectories with randomly selected BC parameters from  
433 the 110 points, with nominal SVM parameters  $\xi_{\text{SVM}} = \{1, 1, 1\} \times 10^{-6}$ . Note that although  
434 Fig. 3(c) shows the surface displacements for all ablative components in  $\mathcal{D}_1$ , only the *surface*

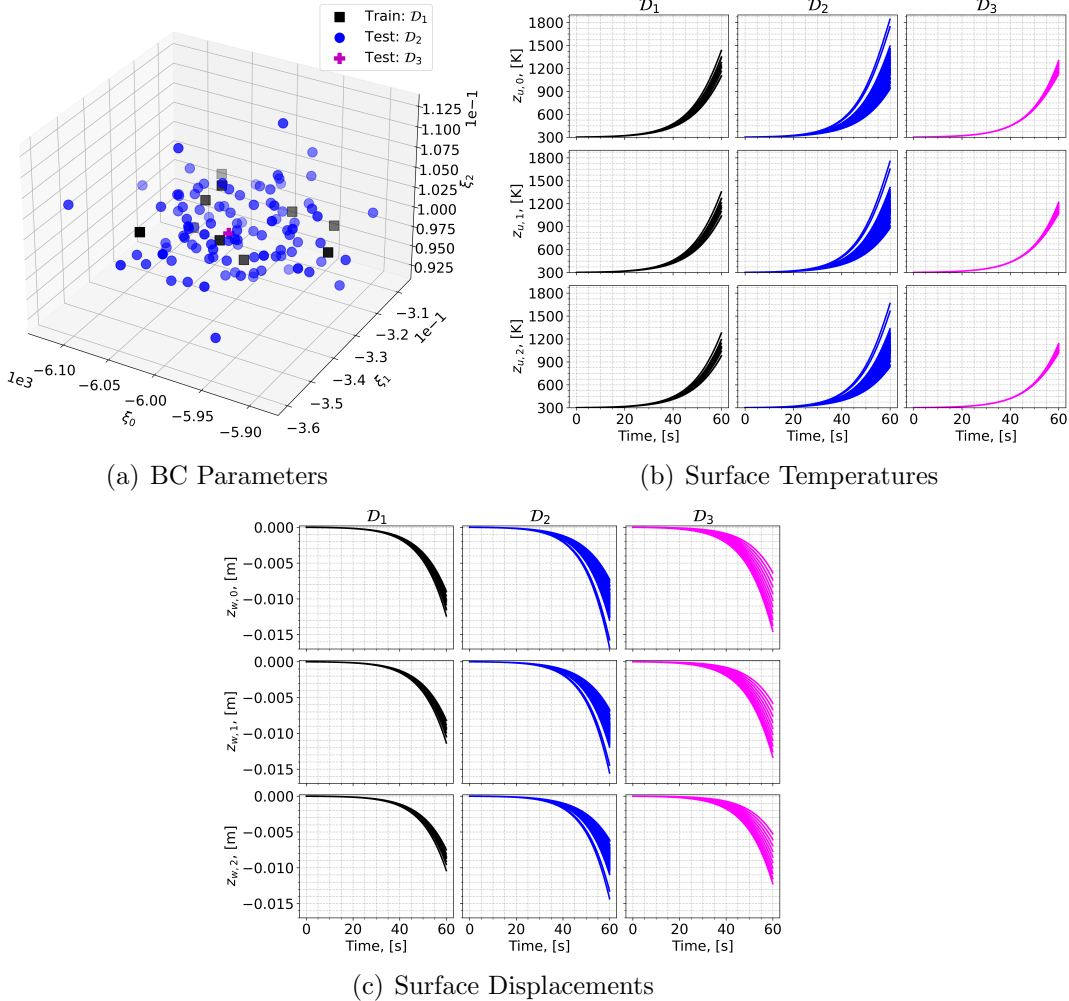


Figure 3: Boundary condition parameters, temperature observables, and displacement observables for the training and testing datasets.

435 temperature is used for training the PIROM.

436 Two additional datasets are generated for testing. The dataset  $\mathcal{D}_2$  includes the remaining  
 437 100 BC parameter values not considered in  $\mathcal{D}_1$ , and the high-fidelity simulation are generated  
 438 with the same nominal SVM parameters. The cases in the  $\mathcal{D}_3$  fixes the boundary condition  
 439 as shown in Fig. 3(a) and varies the SVM parameters as shown in Table. **x**. The testing  
 440 datasets  $\mathcal{D}_2$  and  $\mathcal{D}_3$  are *out-of-distribution* (OOD) datasets, and are meant for testing the  
 441 generalizability of the ROMs to unseen BCs and SVMs, respectively.

## 442 4.4 Performance Metrics

443 The performance of the PIROM is evaluated by the metrics of prediction error and compu-  
 444 tational cost.

445 **Prediction Error** Consider one trajectory of high-fidelity surface temperature and dis-  
 446 placement data  $\left\{ \left( t_k, \mathbf{z}_{u,\text{HF}}^{(l)}(t_k), \mathbf{z}_{w,\text{HF}}^{(l)}(t_k) \right) \right\}_{k=0}^{p-1}$  for the  $l$ -th operating condition in the testing  
 447 datasets  $\mathcal{D}_2$  or  $\mathcal{D}_3$ . The difference  $e_i^{(l)}$  for the  $i$ -th predicted observable, denoted as  $z_i^{(l)}$ , is  
 448 computed as,

$$e_i^{(l)} = \frac{1}{\Delta z_i^{(l)}} \sqrt{\frac{1}{p} \sum_{k=0}^{p-1} \left( z_{i,\text{HF}}^{(l)}(t_k) - z_i^{(l)}(t_k) \right)^2} \quad (48)$$

449 for  $i = 1, 2, 3$  and  $z_i^{(l)} \in \left\{ z_{i,u}^{(l)}, z_{i,w}^{(l)} \right\}$ , and where,

$$\Delta z_i^{(l)} = \max_{0 \leq k \leq p-1} z_{i,\text{HF}}^{(l)}(t_k) - \min_{0 \leq k \leq p-1} z_{i,\text{HF}}^{(l)}(t_k) \quad (49)$$

450 Subsequently, the prediction error of one trajectory is computed by a weighted sum based  
 451 on the area of each *ablative component*, resulting in the normalized root mean square error  
 452 (NRMSE) metric for one trajectory,

$$\text{NRMSE} = \frac{\sum_{i=1}^{\tilde{N}} |\Omega_i| e_i^{(l)}}{\sum_{i=1}^{\tilde{N}} |\Omega_i|} \times 100\% \quad (50)$$

453 For one dataset, the NRMSE is defined to be the average of the NRMSEs of all trajectories  
 454 in the dataset.

455 **Computational Acceleration** The *computational acceleration* metric focuses on the quan-  
 456 tification of the speedup factor  $\frac{\mathcal{T}_{\text{HF}}(\mathcal{D})}{\mathcal{T}_{\mathcal{M}}(\mathcal{D})}$ , where  $\mathcal{T}_{\text{HF}}(\mathcal{D})$  and  $\mathcal{T}_{\mathcal{M}}(\mathcal{D})$  correspond to the wall-clock  
 457 time required by the high-fidelity model and the reduced-order model  $\mathcal{M}$  (i.e., PIROM or  
 458 RPM) to evaluate all trajectories in the dataset  $\mathcal{D}$ , respectively. For a benchmark analysis  
 459 of the computational costs during the training phase, please refer to Ref. [12]. All computa-

460 tions are performed in serial for fairness in an Intel Xeon (R) Gold 6258R CPU 2.70GHz  
461 computer with 62 GB of RAM.

## 462 4.5 Generalization to Boundary Conditions

463 To investigate the generalization performance on the BCs, the PIROM and RPM are tested  
464 using the  $\mathcal{D}_2$  dataset. Temperature trajectory predictions for one representative test case  
465 are shown in Figs. 4(a) and 4(b), where the PIROM accurately captures the temperature  
466 and displacement dynamics. The RPM exhibits larger deviations of surface temperature and  
467 displacements, and under-predicts the surface displacements due to the averaging effect of  
468 the LCM. The mean NRMSE across all test cases in  $\mathcal{D}_2$  is shown in Figs. 4(e) and 4(f), where  
469 the PIROM consistently achieves errors below 1% for both temperature and displacement  
470 predictions, and improves the RPM’s accuracy by an order of magnitude.

471 The average temperature for the substrate component is shown in Fig. 4(e). As, expected,  
472 the LCM computes highly accurate predictions for the substrate’s average temperature due  
473 to the symmetric nature of the TPS configuration. Despite the PIROM being trained on  
474 the surface temperatures for the three ablative components, the PIROM retains the LCM’s  
475 accuracy for the substrate’s average temperature. This results demonstrates the PIROM’s  
476 ability to generalize to untrained observables while preserving the underlying physics of the  
477 reduced-physics backbone.

## 478 4.6 Generalization to Surface Velocity Models

479 The generalization performance of the PIROM and RPM is also evaluated on surface velocity  
480 models using the  $\mathcal{D}_3$  dataset. As detailed in Table x, the SVM parameters in  $\mathcal{D}_3$  are  
481 perturbed 10 times by up to  $\pm 50\%$  from their nominal values. The

<sup>482</sup> **4.7 Computational Cost**

<sup>483</sup> **4.8 Summary of Results**

<sup>484</sup> **5 Conclusions**

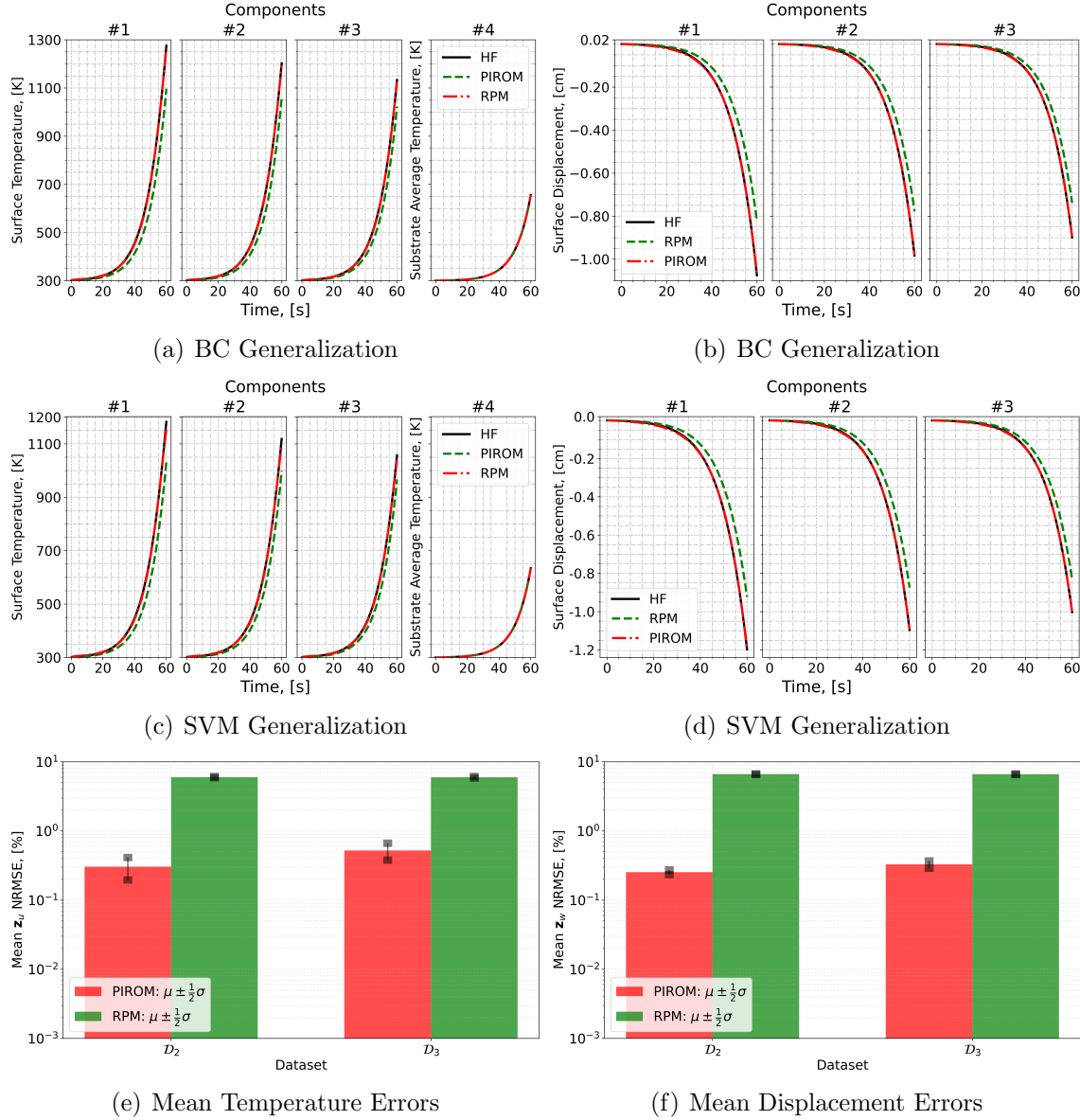


Figure 4: PIROM predictions against high-fidelity solutions for (a)-(b) BC generalization, (c)-(d) SVM generalization, and (e)-(f) mean errors across testing datasets.

## 485 A Technical Details

486 This appendix presents the technical details of the PIROM framework applied to the TPS  
487 ablation problem. The first section provides the mathematical details for the definition of  
488 the DG-FEM. The second section follows the projection procedures from Ref. [\[x\]](#), and demon-  
489 strates the effects of coarse-graining on the advection matrix. The third section presents the  
490 derivation of the LCM model from an energy-conservation perspective.

### 491 A.1 Full-Order Model

492 To obtain the full-order numerical solution, the governing equation is spatially discretized  
493 using variational principles of Discontinuous Galerkin (DG) to result in a high-dimensional  
494 system of ordinary differential equations (ODEs). The DG-FEM model is written in an  
495 element-wise form, which is beneficial for subsequent derivations of the lower-order models.  
496 Note that the choice of DG approach here is mainly for theoretical convenience in the sub-  
497 sequent coarse-graining formulation. In the numerical results, the full-order TPS ablation  
498 simulations is computed using standard FEM instead, and the equivalence between DG and  
499 standard FEM is noted upon their convergence.

#### 500 A.1.1 Domain Discretization

501 Consider a conforming mesh partition of the domain, as shown in Fig. [DOMAIN](#), where each  
502 element belongs to one and only one component. Denote the collection of all  $M$  elements  
503 as  $\{E_i\}_{i=1}^M$ . To ease the description of the DG model, a graph structure is employed. The  
504 elements are treated as vertices, the set of which is denoted  $\mathcal{V} = \{m\}_{m=1}^M$ . Two neighboring  
505 elements,  $E_i$  and  $E_j$ , are connected by an edge  $(i, j)$ , and the shared boundary between them  
506 is denoted  $e_{ij}$ . The collection of all edges are denoted  $\mathcal{E}$ , and  $\mathcal{G}$  is referred to as a graph.  
507 In the graph, the edges are unidirected, meaning if  $(i, j) \in \mathcal{E}$  then  $(j, i) \in \mathcal{E}$ . Furthermore,  
508 denote the neighbors of the  $i$ -th element as  $\mathcal{N}_i = \{j | (i, j) \in \mathcal{E}\}$ . Lastly, for the ease of

509 notation, introduce two special indices:  $T$  for the boundary of an element that overlaps with  
 510 the Dirichlet boundary condition, and similarly  $q$  for the Neumann boundary condition.

### 511 A.1.2 Weak Form of Discontinuous Galerkin Method

512 Choosing appropriate basis functions  $\phi_k$  and  $\phi_l$  and using the Interior Penalty Galerkin  
 513 (IPG) scheme [5], the variational bilinear form for eq. (1a) is,

$$\sum_{i=1}^M a_{\epsilon,i}(\phi_k, \phi_l) = \sum_{i=1}^M L_i(\phi_k) \quad (51)$$

514 where  $\epsilon$  is an user-specified parameter and,

$$a_{\epsilon,i}(\phi_k, \phi_l) = \int_{E^{(i)}} \left( \rho c_p \phi_k \frac{\partial \phi_l}{\partial t} + \nabla \phi_k \cdot (\mathbf{k} \nabla \phi_l) - \rho c_p \phi_k \mathbf{v} \cdot \nabla \phi_l \right) dE^{(i)} \quad (52a)$$

$$\begin{aligned} &= - \sum_{j \in \mathcal{N}_i \cup \{T_b\}} \int_{e_{ij}} \{ \mathbf{k} \nabla \phi_k \cdot n \} [\phi_l] de_{ij} + \epsilon \sum_{j \in \mathcal{N}_i \cup \{T_b\}} \int_{e_{ij}} \{ \mathbf{k} \nabla \phi_l \cdot n \} [\phi_k] de_{ij} \\ &\quad + \sigma \sum_{j \in \mathcal{N}_i \cup \{T_b\}} \int_{e_{ij}} [\phi_k] [\phi_l] de_{ij} \end{aligned} \quad (52b)$$

$$L_i(v) = \epsilon \sum_{j \in \mathcal{N}_i \cup \{T_b\}} \int_{e_{ij}} (\mathbf{k} \nabla \phi_l \cdot n) T_b de_{ij} + \int_{e_{iq}} \phi_k q_b de_{iq} + \sigma \int_{e_{iT}} \phi_k T_b de_{iT} \quad (52c)$$

515 In the bi-linear form above, the notations  $[]$  and  $\{ \}$  are respectively the jumps and averages  
 516 at the boundary  $e_{ij}$  share by two elements  $E_i$  and  $E_j$ ,

$$[u] = u|_{E_i} - u|_{E_j}, \quad \{u\} = \frac{1}{2} \left( u|_{E_i} + u|_{E_j} \right), \quad \text{for } x \in e_{ij} = E_i \cap E_j$$

517 Furthermore, in the bi-linear form, the terms associated with  $\sigma$  are introduced to enforce  
 518 the Dirichlet boundary conditions;  $\sigma$  is a penalty factor whose value can depend on the size  
 519 of an element. Depending on the choice of  $\epsilon$ , the bi-linear form corresponds to symmetric  
 520 IPG ( $\epsilon = -1$ ), non-symmetric IPG ( $\epsilon = 1$ ), and incomplete IPG ( $\epsilon = 0$ ). All these schemes  
 521 are consistent with the original PDE and have similar convergence rate with respect to mesh

522 size. In the following derivations, the case  $\epsilon = 0$  is chosen for the sake of simplicity.

### 523 A.1.3 Discontinuous Galerkin Model

524 Next, the DG-based model is written in an element-wise form. For the  $i$ -th element, use a  
525 set of  $P$  trial functions to represent the temperature as in eq. (6). Without loss of generality,  
526 the trial functions are assumed to be orthogonal, so that  $\int_{E^{(i)}} \phi_k^{(i)}(x) \phi_l^{(i)}(x) dx = |E^{(i)}| \delta_{kl}$ ,  
527 where  $|E^{(i)}|$  is the area ( $n_d = 2$ ) or volume ( $n_d = 3$ ) of the  $i$ -th element, and  $\delta_{kl}$  is the  
528 Kronecker delta.

529 Using test functions same as trial functions, the dynamics  $\mathbf{u}^{(i)}$  is obtained by evaluating  
530 the element-wise bi-linear forms,

$$a_{\epsilon,i}(\phi_k^{(i)}, T^{(i)}) = L_i(\phi_k^{(i)}), \quad k = 1, 2, \dots, P \quad (53)$$

531 The above procedure yields,

$$\mathbf{A}^{(i)} \dot{\mathbf{u}}^{(i)} = (\mathbf{B}^{(i)} + \mathbf{C}^{(i)}(t)) \mathbf{u}^{(i)} + \sum_{j \in \mathcal{N}_i \cup \{T_b\}} \left( \mathbf{B}_{ij}^{(i)} \mathbf{u}^{(i)} + \mathbf{B}_{ij}^{(j)} \mathbf{u}^{(j)} \right) + \mathbf{f}^{(i)}(t) \quad (54)$$

532 where for  $k, l = 1, 2, \dots, P$ ,

$$[\mathbf{A}^{(i)}]_{kl} = \int_{E^{(i)}} \rho c_p \phi_k^{(i)} \phi_l^{(i)} dE^{(i)} \quad (55a)$$

$$[\mathbf{B}^{(i)}]_{kl} = - \int_{E^{(i)}} (\nabla \phi_k^{(i)}) \cdot (\mathbf{k} \nabla \phi_l^{(i)}) dE^{(i)} \quad (55b)$$

$$[\mathbf{C}^{(i)}]_{kl} = \int_{E^{(i)}} \rho c_p \phi_k^{(i)} \mathbf{v}^{(i)} \cdot \nabla \phi_l^{(i)} dE^{(i)} \quad (55c)$$

$$[\mathbf{B}_{ij}^{(i)}] = \int_{e_{ij}} \left\{ \mathbf{k} \nabla \phi_k^{(i)} \cdot \hat{n} \right\} \phi_l^{(i)} - \sigma [\phi_k^{(i)}] \phi_l^{(i)} de_{ij} \quad (55d)$$

$$[\mathbf{B}_{ij}^{(j)}] = \int_{e_{ij}} - \left\{ \mathbf{k} \nabla \phi_k^{(i)} \cdot \hat{n} \right\} \phi_l^{(j)} + \sigma [\phi_k^{(i)}] \phi_l^{(j)} de_{ij} \quad (55e)$$

$$[\mathbf{f}^{(i)}]_k = \int_{e_{iq}} \phi_k^{(i)} q_b de_{iq} + \sigma \int_{e_{iT}} \phi_k^{(i)} de_{iT} \quad (55f)$$

533 The matrices  $\mathbf{A}^{(i)} \in \mathbb{R}^{P \times P}$ ,  $\mathbf{B}^{(i)} \in \mathbb{R}^{P \times P}$ , and  $\mathbf{C}^{(i)} \in \mathbb{R}^{P \times P}$  are respectively the capacitance,  
 534 conductivity, and advection matrices for element  $i$ . These matrices depend on  $\rho$ ,  $c_p$ ,  $\mathbf{k}$ , and  
 535  $\mathbf{v}$ , and hence can be non-linear functions of  $\mathbf{u}^{(i)}$ . Since the trial functions are orthogonal, if  
 536  $\rho c_p$  is constant within an element,  $\mathbf{A}^{(i)}$  is diagonal; otherwise,  $\mathbf{A}_i$  is symmetric and positive  
 537 definite as  $\rho c_p > 0$ .

538 For compactness, the element-wise model in eq. (54) is also written in matrix form,

$$\mathbf{A}(\dot{\mathbf{u}}) = [\mathbf{B}(\mathbf{u}) + \mathbf{C}(\mathbf{u})] \mathbf{u} + \mathbf{f}(t) \quad (56)$$

539 where  $\mathbf{u} = [\mathbf{u}^{(1)}, \mathbf{u}^{(2)}, \dots, \mathbf{u}^{(M)}]^T \in \mathbb{R}^{MP}$  includes all DG variables,  $\mathbf{f} = [\mathbf{f}^{(1)}, \mathbf{f}^{(2)}, \dots, \mathbf{f}^{(M)}]^T \in$   
 540  $\mathbb{R}^{MP}$ ,  $\mathbf{A}$  and  $\mathbf{C}$  are matrices of  $M$  diagonal blocks whose  $i$ -th blocks are  $\mathbf{A}^{(i)}$  and  $\mathbf{C}^{(i)}$ , and  
 541  $\mathbf{B}$  is a matrix of  $M \times M$  blocks whose  $(i, j)$ -th block is,

$$\mathbf{B}_{ij} = \begin{cases} \mathbf{B}^{(i)} + \sum_{j \in \mathcal{N}_i \cup \{T_b\}} \mathbf{B}_{ij}^{(i)}, & i = j \\ \mathbf{B}_{ij}^{(j)}, & i \neq j \end{cases} \quad (57)$$

542 The dependency of  $\mathbf{A}$ ,  $\mathbf{B}$ , and  $\mathbf{C}$  on  $\mathbf{u}$  is explicitly noted in eq. (56), which is the source of  
 543 non-linearity in the current TPS problem. Moreover, the mesh velocity  $\mathbf{v}$  varies with space  
 544 and time, and thus the advection matrix  $\mathbf{C}$  varies with time as a function of  $q_b$ .

## 545 A.2 Coarse-Graining of Dynamics

546 The LCM is obtained by coarse-graining the full-order DG-FEM. This coarse-graining proce-  
 547 dure produces resolved  $\mathbf{r}^{(1)}(\mathbf{u}, t)$  and residual  $\mathbf{r}^{(2)}(\mathbf{u}, t)$  dynamics as in eq. (23). This section  
 548 presents the detail derivations and magnitude analysis for the resolved and residual dynam-  
 549 ics.

550 **A.2.1 Resolved Dynamics**

551 Using eq. (20), the resolved dynamics is computed as follows,

$$\mathbf{r}^{(1)}(\mathbf{u}, t) = \mathcal{P} [\Phi^+ \mathbf{A}(\mathbf{u})^{-1} (\mathbf{B}(\mathbf{u})\mathbf{u} + \mathbf{C}(\mathbf{u})\mathbf{u} + \mathbf{f}(t))] \quad (58a)$$

$$\begin{aligned} &= \Phi^+ \mathbf{A}(\mathbf{P}\mathbf{u})^{-1} \mathbf{P}\mathbf{B}(\mathbf{P}\mathbf{u}) \mathbf{P}\mathbf{u} + \Phi^+ \mathbf{A}(\mathbf{P}\mathbf{u})^{-1} \mathbf{P}\mathbf{C}(\mathbf{P}\mathbf{u}) \mathbf{P}\mathbf{u} \\ &\quad + \Phi^+ \mathbf{A}(\mathbf{P}\mathbf{u})^{-1} \mathbf{P}\mathbf{f}(t, \mathbf{P}\mathbf{u}) \end{aligned} \quad (58b)$$

$$\begin{aligned} &= \underbrace{\Phi^+ \mathbf{A}(\Phi\bar{\mathbf{u}})^{-1} \Phi}_{\#1} \underbrace{\Phi^+ \mathbf{B}(\Phi\bar{\mathbf{u}}) \Phi\bar{\mathbf{u}}}_{\#2} + \Phi^+ \mathbf{A}(\Phi\bar{\mathbf{u}})^{-1} \Phi \underbrace{\Phi^+ \mathbf{C}(\Phi\bar{\mathbf{u}}) \Phi\bar{\mathbf{u}}}_{\#3} \\ &\quad + \Phi^+ \mathbf{A}(\Phi\bar{\mathbf{u}})^{-1} \Phi \underbrace{\Phi^+ \mathbf{f}(t, \Phi\bar{\mathbf{u}})}_{\#4} \end{aligned} \quad (58c)$$

552 Detailed derivations for the #1, #2, and #4 terms can be found in Ref. [x]. The effects of  
553 coarse-graining on the advection term #3 are analyzed next.

554 **Term #3** The  $\mathbf{C}(\mathbf{u}) \in \mathbb{R}^{MP \times MP}$  matrix contains  $M$  diagonal of size  $P \times P$ , since the  
555 basis functions are defined locally on each element. Therefore,  $[\mathbf{C}(\mathbf{u})]_{ij} = \mathbf{0}$  for all  $i \neq j$  with  
556  $i, j = 1, 2, \dots, M$ . It follows that for  $k, l = 1, 2, \dots, N$ ,

$$[\Phi^+ \mathbf{C}(t, \Phi\bar{\mathbf{u}}) \Phi]_{kl} = \sum_{i=1}^M \sum_{j=1}^M \boldsymbol{\varphi}_i^{k+} [\mathbf{C}(t, \Phi\bar{\mathbf{u}})]_{ij} \boldsymbol{\varphi}_j^l \quad (59a)$$

$$= \sum_{i=1}^M \boldsymbol{\varphi}_i^{k+} [\mathbf{C}(t, \Phi\bar{\mathbf{u}})]_{ii} \boldsymbol{\varphi}_i^l \quad (59b)$$

$$= \sum_{i \in \mathcal{V}_k} \boldsymbol{\varphi}_i^{k+} [\mathbf{C}(t, \Phi\bar{\mathbf{u}})]_{ii} \boldsymbol{\varphi}_i^l \quad (59c)$$

557 where in the second row, the fact that  $[\mathbf{C}(\mathbf{u})]_{ij} = 0$  for all  $i \neq j$  is used, and in the last row,  
558 the fact that  $\boldsymbol{\varphi}_i^{k+} = 0$  for all  $i \notin \mathcal{V}_k$  is used. Now, considering that  $[\mathbf{C}(\mathbf{u})]_{ii}$  has a (1, 1)-th  
559 zero element, i.e.,  $[\mathbf{C}(t, \Phi\bar{\mathbf{u}})]_{ii} = 0$ , and that if  $k \neq l$  then  $i \notin \mathcal{V}_l$  and thus  $\boldsymbol{\varphi}_i^l = \mathbf{0}$ , it follows

560 that for some index  $i \in \mathcal{V}_k$ ,

$$\boldsymbol{\varphi}_i^{k+} [\mathbf{C}(t, \Phi \bar{\mathbf{u}})]_{ii} \boldsymbol{\varphi}_i^l = \boldsymbol{\varphi}_i^{k+} [\mathbf{C}(t, \Phi \bar{\mathbf{u}})]_{ii} \boldsymbol{\varphi}_i^k = \frac{|E_i|}{|\Omega_k|} [C_{11}(t, \Phi \bar{\mathbf{u}})]_{ii} = 0 \quad (60)$$

561 The matrix  $[\Phi^+ \mathbf{C}(t, \Phi \bar{\mathbf{u}}) \Phi]_{kl} = 0$  for all  $k, l = 1, 2, \dots, N$ , and thus,

$$\bar{\mathbf{C}}(t, \bar{\mathbf{u}}) = \Phi^+ \mathbf{C}(t, \Phi \bar{\mathbf{u}}) \Phi = \mathbf{0} \quad (61)$$

562 as indicated by the LCM in eq. (9).

### 563 A.2.2 Magnitude Analysis for Residual Dynamics

564 Next, the magnitude of the residual dynamics  $\mathbf{r}^{(2)}(\mathbf{u}, t)$  is analyzed to pinpoint the missing  
565 physics in the LCM. By definition,

$$\mathbf{r}^{(2)}(\mathbf{u}, t) = \dot{\bar{\mathbf{u}}} - \mathbf{r}^{(1)}(\bar{\mathbf{u}}, t) \quad (62a)$$

$$= \Phi^+ \mathbf{r}(\mathbf{u}, t) - \mathbf{r}^{(1)}(\mathbf{u}, t) \quad (62b)$$

$$\begin{aligned} &= \underbrace{\Phi^+ \mathbf{A}(\mathbf{u})^{-1} \mathbf{B}(\mathbf{u}) \mathbf{u} - \bar{\mathbf{A}}(\bar{\mathbf{u}})^{-1} \bar{\mathbf{B}}(\bar{\mathbf{u}}) \bar{\mathbf{u}}}_{\#1} + \underbrace{\Phi^+ \mathbf{A}(\mathbf{u})^{-1} \mathbf{C}(\mathbf{u}) \mathbf{u} - \bar{\mathbf{A}}(\bar{\mathbf{u}})^{-1} \bar{\mathbf{C}}(t, \bar{\mathbf{u}}) \bar{\mathbf{u}}}_{\#2} \\ &\quad + \underbrace{\Phi^+ \mathbf{A}(\mathbf{u})^{-1} \mathbf{f}(t) - \bar{\mathbf{A}}(\bar{\mathbf{u}})^{-1} \bar{\mathbf{f}}(t)}_{\#3} \end{aligned} \quad (62c)$$

566 The magnitude analysis for terms  $\#1$  and  $\#3$  can be found in Ref. [\[x\]](#). The analysis for term  
567  $\#2$  is presented next. Let  $\mathbf{D}(\bar{\mathbf{u}}) = \mathbf{A}(\Phi \bar{\mathbf{u}})^{-1} \mathbf{P} \mathbf{C}(t, \Phi \bar{\mathbf{u}})$ , then,

$$\Phi^+ \mathbf{A}(\mathbf{u})^{-1} \mathbf{C}(\mathbf{u}) \mathbf{u} - \bar{\mathbf{A}}(\bar{\mathbf{u}})^{-1} \bar{\mathbf{C}}(t, \bar{\mathbf{u}}) \bar{\mathbf{u}} \quad (63a)$$

$$= \Phi^+ \mathbf{A}(\mathbf{u})^{-1} \mathbf{C}(\mathbf{u}) \mathbf{u} - \Phi^+ \mathbf{A}(\Phi \bar{\mathbf{u}})^{-1} \mathbf{P} \mathbf{C}(t, \Phi \bar{\mathbf{u}}) \Phi \Phi^+ \mathbf{u} \quad (63b)$$

$$= \Phi^+ \mathbf{A}^{-1}(\mathbf{u}) \mathbf{C}(\mathbf{u}) \mathbf{u} - \Phi^+ \mathbf{D}(\bar{\mathbf{u}}) \Phi \Phi^+ \mathbf{u} \quad (63c)$$

$$(63d)$$

568 where  $\mathbf{P} = \Phi\Phi^+$ . Thus,

$$\|\Phi^+\mathbf{A}(\mathbf{u})^{-1}\mathbf{C}(\mathbf{u})\mathbf{u} - \bar{\mathbf{A}}^{-1}(\bar{\mathbf{u}})\bar{\mathbf{C}}(t, \bar{\mathbf{u}})\bar{\mathbf{u}}\| \quad (64a)$$

$$\leq \|\Phi^+\mathbf{A}^{-1}(\mathbf{u})\mathbf{C}(\mathbf{u})\mathbf{u} - \Phi^+\mathbf{D}(\bar{\mathbf{u}})\mathbf{u}\| + \|\Phi^+\mathbf{D}(\bar{\mathbf{u}})\mathbf{u} - \Phi^+\mathbf{D}(\bar{\mathbf{u}})\Phi\Phi^+\mathbf{u}\| \quad (64b)$$

$$\leq \|\Phi^+\| \underbrace{\|\mathbf{A}^{-1}(\mathbf{u})\mathbf{C}(\mathbf{u})\mathbf{u} - \mathbf{D}(\bar{\mathbf{u}})\mathbf{u}\|}_{\#1} + \|\Phi^+\mathbf{D}(\bar{\mathbf{u}})\| \underbrace{\|\mathbf{u} - \Phi\Phi^+\mathbf{u}\|}_{\#2} \quad (64c)$$

569 where term  $\#2$  is due to the appriximation of non-uniform temperaeture as constants, and  
 570 term  $\#1$  is the error in the advection dynamics due to coarse-graining.

### 571 A.3 Lumped Capacitance Model

572 The following assumptions are employed: (1) the temperature in component  $(i)$  is described  
 573 by a scalar time-varying average temperature  $\bar{u}^{(i)}$ , (2) between neighboring components  $(i)$   
 574 and  $(j)$  the heat flux is approximated as,

$$q_{ij} = \frac{\bar{u}^{(j)} - \bar{u}^{(i)}}{R_{ij}} \quad (65)$$

575 where  $R_{ij}$  is the thermal resistance. Empirically, for a component of isotropic heat conduc-  
 576 tivity  $k$ , length  $\ell$ , and cross-section area  $A$ , the thermal resistance is  $R = \ell/kA$ . Between  
 577 components  $i$  and  $j$ , define  $R_{ij} = R_i + R_j$ . In addition, the heat flux due to Dirichlet  
 578 boundary condition is computed as  $q_{iT} = (T_b - \bar{u}^{(i)})/R_i$ .

579 At component  $i$ , the dynamics of LCM are given by,

$$\int_{E^{(i)}} \rho c_p \dot{\bar{u}}^{(i)} dE^{(i)} = \left( \sum_{j \in \mathcal{N}_i} \int_{e_{ij}} \frac{\bar{u}^{(j)} - \bar{u}^{(i)}}{R_{ij}} de_{ij} \right) + \int_{e_{iq}} q_b de_{iq} + \int_{e_{iT}} \frac{T_b - \bar{u}^{(i)}}{R_i} de_{iT} \quad (66a)$$

$$\bar{A}^{(i)} \dot{\bar{u}}^{(i)} = \left( \sum_{j \in \mathcal{N}_i} \frac{|e_{ij}|}{R_{ij}} (\bar{u}^{(j)} - \bar{u}^{(i)}) \right) + |e_{iq}| \bar{q}^{(i)} + \frac{|e_{iT}|}{R_i} (\bar{T}^{(i)} - \bar{u}^{(i)}) \quad (66b)$$

$$= \sum_{j \in \mathcal{N}_i} \left( -\frac{|e_{ij}|}{R_{ij}} \bar{u}^{(i)} + \frac{|e_{ij}|}{R_{ij}} \bar{u}^{(j)} \right) + \left( -\frac{|e_{iT}|}{R_i} \bar{u}^{(i)} \right) + \left( |e_{iq}| \bar{q}^{(i)} + \frac{|e_{iT}|}{R_i} \bar{T}^{(i)} \right) \quad (66c)$$

$$= \sum_{j \in \mathcal{N}_i \cup \{T_b\}} \left( \bar{B}_{ij}^{(i)} \bar{u}^{(i)} + \bar{B}_{ij}^{(j)} \bar{u}^{(j)} \right) + \bar{f}^{(i)} \quad (66d)$$

580 where in eq. (66b)  $|e|$  denotes the length ( $d = 2$ ) or area ( $d = 3$ ) of a component boundary  
 581  $e$ . The  $\bar{A}^{(i)}$ ,  $\bar{B}_{ij}^{(i)}$ , and  $\bar{B}_{ij}^{(j)}$  quantities are provided in eq. (12).

582 The lumped-mass representation for the four-component TPS is shown in Fig. ???. Let  
 583  $v_i$  represent the area of the  $i$ -th element,  $\bar{\rho c_p}_i$ , the heat capacity evaluated using the average  
 584 temperature  $\bar{u}^{(i)}$ , and  $1/R_{ij} = 1/R_i(\bar{u}^{(i)}) + 1/R_j(\bar{u}^{(j)})$  the equivalent thermal resistance  
 585 between elements  $i$  and  $j$ . Leveraging the formulas from eqs. (11b) and (12), the LCM  
 586 matrices are given by,

$$\bar{\mathbf{A}} = \begin{bmatrix} \bar{\rho c_p}_1 v_1 & 0 & 0 & 0 \\ 0 & \bar{\rho c_p}_2 v_2 & 0 & 0 \\ 0 & 0 & \bar{\rho c_p}_3 v_3 & 0 \\ 0 & 0 & 0 & \bar{\rho c_p}_4 v_4 \end{bmatrix}, \quad (67a)$$

$$\bar{\mathbf{B}} = \begin{bmatrix} \frac{1}{R_{12}} + \frac{1}{R_{14}} & -\frac{1}{R_{12}} & 0 & -\frac{1}{R_{14}} \\ -\frac{1}{R_{12}} & \frac{1}{R_{12}} + \frac{1}{R_{24}} + \frac{1}{R_{23}} & -\frac{1}{R_{23}} & -\frac{1}{R_{24}} \\ 0 & -\frac{1}{R_{32}} & \frac{1}{R_{32}} + \frac{1}{R_{34}} & -\frac{1}{R_{34}} \\ -\frac{1}{R_{14}} & -\frac{1}{R_{24}} & -\frac{1}{R_{34}} & \frac{1}{R_{14}} + \frac{1}{R_{24}} + \frac{1}{R_{34}} \end{bmatrix}, \quad \bar{\mathbf{f}} = \begin{bmatrix} \bar{q}^{(1)} \\ \bar{q}^{(2)} \\ \bar{q}^{(3)} \\ 0 \end{bmatrix} \quad (67b)$$

587 **References**

- 588 [1] Adam J. Amar, A. Brandon Oliver, Benjamin S. Kirk, Giovanni Salazar, and Justin  
589 Droba. Overview of the charring ablator response (char) code. In AIAA, editor, *AIAA*  
590 *Aviation Forum*, 2016.
- 591 [2] Guy L. Bergel, Frank B. Beckwith, Gabel J. de Frias, Kevin M. Manktelow, Mark T.  
592 Merewether, Scott T. Miller, Krishen J. Parmar, Timothy S. Shelton, Jesse T. Thomas,  
593 Jeremy T. Trageser, Benjamin T. Treweek, Michael V. Veilleux, and Ellen B. Wagman.  
594 *Sierra/SolidMechanics 5.6 User's Manual*, 2022.
- 595 [3] Ricky T. Q. Chen, Yulia Rubanova, Jesse Bettencourt, and David Duvenaud. Neural  
596 ordinary differential equations, 2019.
- 597 [4] Jonathan Clausen, Victor Brunini, Lincoln Collins, Robert C Knaus, Alec Kucala,  
598 Stephen Lin, Daniel Robert Moser, Malachi Phillips, Thomas Michael Ransegnola,  
599 Samuel Ramirez Subia, et al. Sierra multimechanics module: Aria verification manual-  
600 version 5.22. Technical report, Sandia National Lab.(SNL-NM), Albuquerque, NM  
601 (United States), 2024.
- 602 [5] Gary Cohen and Sebastien Pernet. *Finite Element and Discontinuous Galerkin Methods*  
603 *for Transient Wave Equations*. Springer Dordrecht, Le Chesnay and Toulouse France,  
604 2018.
- 605 [6] Matthew Gasch, Keith Peterson, Mairead Stackpoole, Ethiraj Venkatapathy, Gregory  
606 Gonzales, and Kyle Hendrickson. Development of advanced ablative carbon phenolic  
607 tps for future nasa missions and commercial space. In *38th Annual Small Satellite*  
608 *Conference*, Logan, Utah, May 2024.
- 609 [7] Frank P. Incropera, David P. DeWitt, Theodore L. Bergman, and Adrienne S. Lavine.  
610 *Fundamentals of Heat and Mass Transfer*. Wiley, Hoboken, NJ, 7th edition, 2011.

- 611 [8] R. J. Klock and Carlos Cesnik. Nonlinear thermal reduced-order modeling for hypersonic  
612 vehicles. *AIAA Journal*, 55(7), 2017.
- 613 [9] Eric Parish and Karthik Duraisamy. Non-markovian closure models for large eddy  
614 simulations using the mori-zwanzig formalism. *Phys. Rev. Fluids*, 2:014604, Jan 2017.
- 615 [10] Eric Parish and Karthik Duraisamy. A unified framework for multiscale modeling using  
616 the mori-zwanzig formalism and the variational multiscale method. *ArXiv*, 12 2017.
- 617 [11] Eric Parish and Karthik Duraisamy. *Coarse-Graining Turbulence Using the  
618 Mori-Zwanzig Formalism*. Cambridge University Press, Cambridge, 2025.
- 619 [12] Carlos A. Vargas Venegas, Daning Huang, Patrick Blonigan, and John Tencer. Physics-  
620 infused reduced-order modeling for analysis of multi-layered hypersonic thermal protec-  
621 tion systems. *ArXiv*, 2025.
- 622 [13] Yin Yu, John Harlim, Daning Huang, and Yan Li. Learning coarse-grained dynamics  
623 on graph. *arXiv preprint arXiv:2405.09324*, 2024.